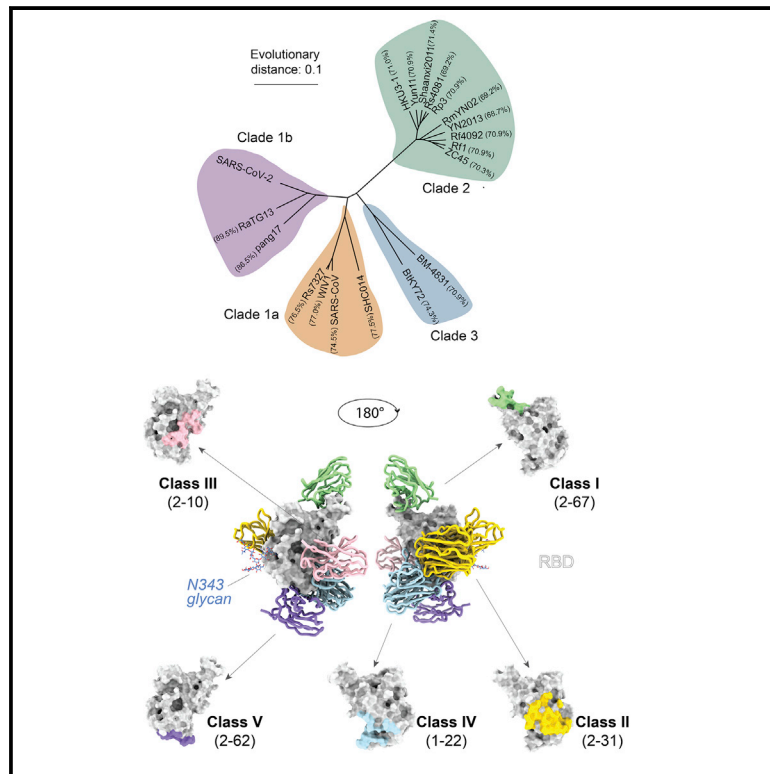**Article**

Superimmunity by pan-sarbecovirus nanobodies

Graphical abstract

Authors

Yufei Xiang, Wei Huang, Hejun Liu, ...,
Ian A. Wilson, Derek J. Taylor, Yi Shi

Correspondence

wally.yis@gmail.com

In brief

Xiang et al. characterize 100 diverse pan-sarbecovirus nanobodies (psNbs) that are highly effective against SARS-CoV and SARS-CoV-2 variants, including Omicron, with the best median neutralization potency at single-digit nanograms per milliliter. Structural determinations of 13 psNbs reveal five RBD epitope classes, providing insights into the mechanisms and evolution of their broad activities.

Highlights

- Discovery of a large repertoire of potent nanobodies against diverse sarbecoviruses

- Structural determinations of 13 psNbs reveal over five broadly neutralizing RBD epitopes

- Highly evolved psNbs target conserved RBD epitopes that are small, flat, and flexible

- The potency of psNbs negatively correlates with the distance of epitopes from the RBS

CellPress

Cell Reports

Article

Superimmunity by pan-sarbecovirus nanobodies

Yufei Xiang,[1,11,12] Wei Huang,[2,12] Hejun Liu,[3,12] Zhe Sang,[4,12] Sham Nambulli,[5,6] Jérôme Tubiana,[7,8]
Kevin L. Williams, Jr.,[5,6] W. Paul Duprex,[5,6] Dina Schneidman-Duhovny,[7] Ian A. Wilson,[3,9] Derek J. Taylor,[2,10]
and Yi Shi[1,4,11,13,*]

[1]Department of Cell Biology, University of Pittsburgh, Pittsburgh, PA 15213, USA
[2]Department of Pharmacology, Case Western Reserve University, Cleveland, OH 44106, USA
[3]Department of Integrative Structural and Computational Biology, Scripps Research, La Jolla, CA 92037, USA
[4]The University of Pittsburgh and Carnegie Mellon University Program for Computational Biology, Pittsburgh, PA 15213, USA
[5]Center for Vaccine Research, University of Pittsburgh, Pittsburgh, PA 15213, USA
[6]Department of Microbiology and Molecular Genetics, University of Pittsburgh, Pittsburgh, PA 15213, USA
[7]School of Computer Science and Engineering, The Hebrew University of Jerusalem, Jerusalem, Israel
[8]Blavatnik School of Computer Science, Tel Aviv University, Tel Aviv, Israel
[9]Skaggs Institute for Chemical Biology, Scripps Research, La Jolla, CA 92037, USA
[10]Department of Biochemistry, Case Western Reserve University, Cleveland, OH 44106, USA
[11]Department of Pharmacological Sciences, Icahn School of Medicine at Mount Sinai, New York, NY 10029, USA
[12]These authors contributed equally
[13]Lead contact
*Correspondence: wally.yis@gmail.com
https://doi.org/10.1016/j.celrep.2022.111004

SUMMARY

Vaccine boosters and infection can facilitate the development of SARS-CoV-2 antibodies with improved potency and breadth. Here, we observe superimmunity in a camelid extensively immunized with the SARS-CoV-2 receptor-binding domain (RBD). We rapidly isolate a large repertoire of specific ultra-high-affinity nanobodies that bind strongly to all known sarbecovirus clades using integrative proteomics. These pan-sarbecovirus nanobodies (psNbs) are highly effective against SARS-CoV and SARS-CoV-2 variants, including Omicron, with the best median neutralization potency at single-digit nanograms per milliliter. A highly potent, inhalable, and bispecific psNb (PiN-31) is also developed. Structural determinations of 13 psNbs with the SARS-CoV-2 spike or RBD reveal five epitope classes, providing insights into the mechanisms and evolution of their broad activities. The highly evolved psNbs target small, flat, and flexible epitopes that contain over 75% of conserved RBD surface residues. Their potencies are strongly and negatively correlated with the distance of the epitopes from the receptor binding sites.

INTRODUCTION

SARS-related coronaviruses (sarbecoviruses), including SARS-CoV and SARS-CoV-2, are among the most pressing threats to global health. The high genetic diversity, frequent recombination, large natural reservoirs, and proximity to heavily populated areas across continents underlie the recurrent zoonotic risks of sarbecoviruses and other circulating coronaviruses (Boni et al., 2020; Meganck and Baric, 2021). Thus, there is an urgent need to develop broad, effective, and complementary interventions against the currently evolving pandemic as well as future threats. Emerging evidence indicates that B cells isolated from convalescent and infected-then-vaccinated individuals continue to evolve, producing antibodies with increased potency against SARS-CoV-2 antigenic drift (Callaway, 2021; Cho et al., 2021; Regev-Yochay et al., 2022; Schmidt et al., 2021; Stamatatos et al., 2021; Wang et al., 2021). Most antibodies target the spike receptor-binding domain (RBD), which dominates immunogenicity and neutralizing activities of convalescent

and vaccinated sera (Piccoli et al., 2020). Only a small number of immunoglobulin G (IgG) antibodies against the large sarbecovirus family have been successfully isolated, with varied breadth and potency (Martinez et al., 2021; Pinto et al., 2020; Rappazzo et al., 2021; Starr et al., 2021; Tortorici et al., 2021) (Hastie et al., 2021). Moreover, an understanding of the full dynamic repertoire of broadly neutralizing antibodies and mechanisms that shape SARS-CoV-2 superimmunity is still lacking (Callaway, 2021).

$V_H H$ antibodies, or nanobodies (Nbs), are natural, monomeric antigen-binding domains from camelid single-chain-only antibodies (Hamers-Casterman et al., 1993; Muyldermans, 2013). Nbs are small ($\sim$15 kDa) and stable and can be rapidly produced from microbes such as *E.coli* or yeast cells. Highly selected Nbs can target viral antigens with high affinity and selectivity. Because of the small size and robustness, they can be easily bioengineered into multivalent constructs to improve functionality. For these reasons, Nbs have emerged as a versatile and cost-effective antiviral agent and can serve as a model system to study circulating antibody repertoires
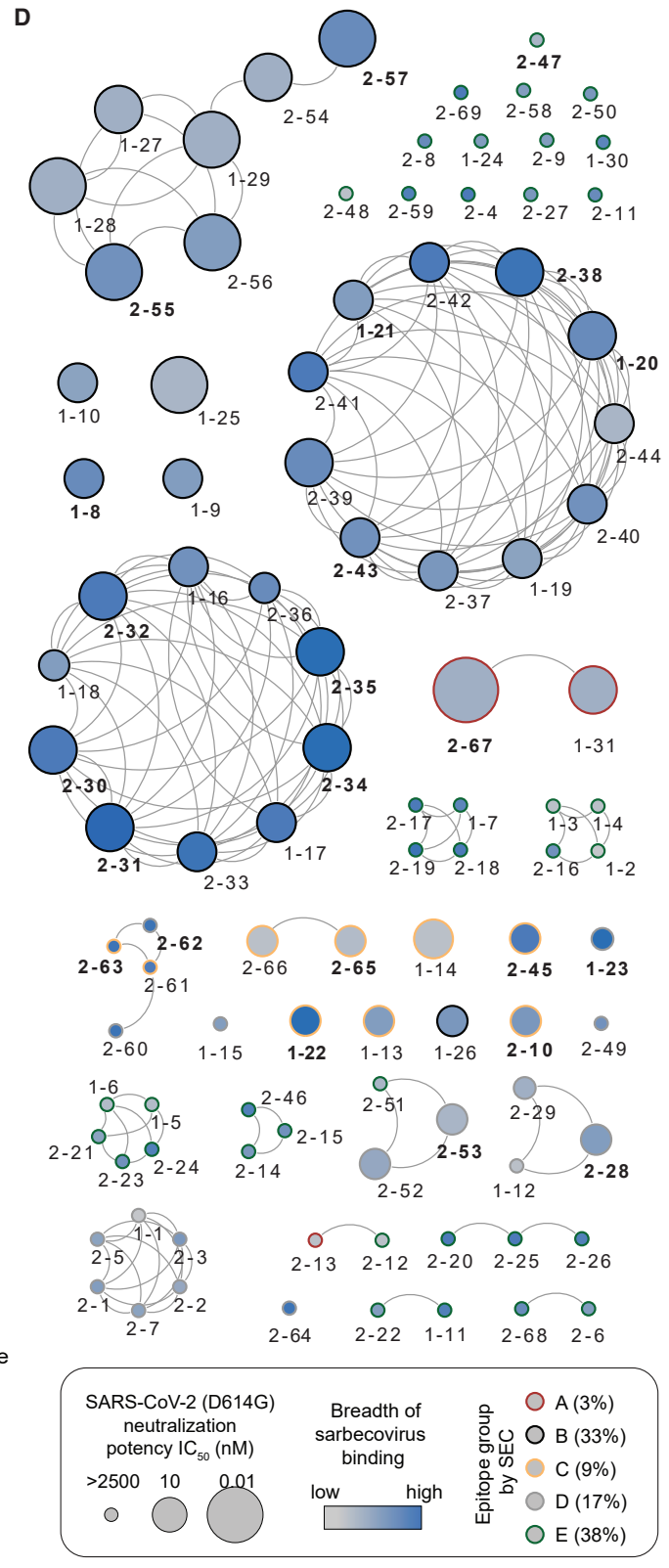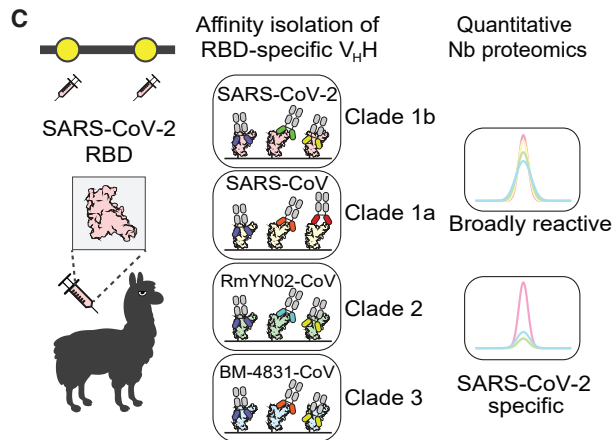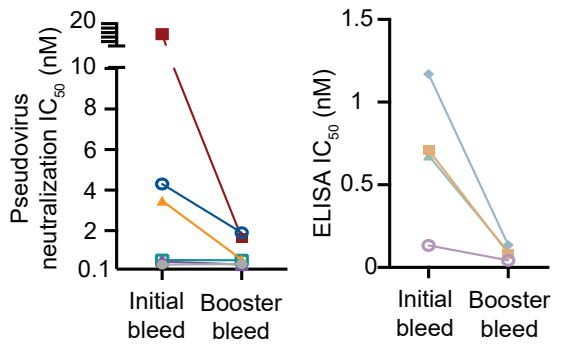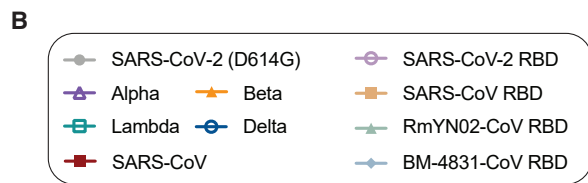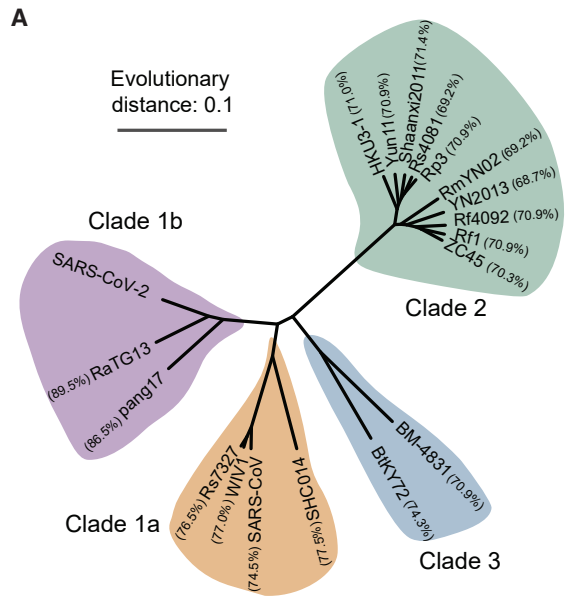
(legend on next page)

(Aria et al., 2022; Detalle et al., 2016; Vanlandschoot et al., 2011; Xiang et al., 2021).

By camelid immunization and proteomics, we recently identified thousands of high-affinity RBD Nbs that potently neutralize SARS-CoV-2 (Xiang et al., 2020). Most ultrapotent Nbs bind the highly variable human ACE2 (hACE2) receptor-binding sites (RBSs) and are therefore less effective against evolving variants. Here, we found that, after immune boosters with recombinant $RBD_{SARS-CoV-2}$, serum V_HH antibodies evolved with substantially improved activities, not only against the variants of concern (VOCs), but also to a broad spectrum of sarbecoviruses (superimmunity). To understand the broad serologic activities, we isolated and systematically characterized 100 high-affinity pan-sarbecovirus Nbs (psNbs) with superior potency and breadth and developed an ultrapotent, bispecific, and aerosolizable psNb (PiN-31). Structural determinations of 13 diverse psNbs with the spike or RBD by cryoelectron microscopy (cryo-EM) and X-ray crystallography revealed five classes with marked diversity within dominant classes. Our analysis offers insights into the remarkable evolution of serologic responses toward broad activity against sarbecoviruses.

RESULTS

Identification and characterization of a large repertoire of potent pan-sarbecovirus Nbs

A llama was initially immunized with a SARS-CoV-2 RBD-Fc fusion protein, and the initial bleed was collected approximately 2 months after priming and three boosts (Xiang et al., 2020). We then re-immunized with four additional boosts for 2 months before the booster bleed was collected (STAR Methods). The polyclonal V_HH mixture of the booster bleed showed higher affinity to $RBD_{SARS-CoV-2}$ (ELISA IC_{50} of 43 pM) compared with that of the initial bleed (IC_{50} of 130 pM) (Figures 1B and S1A). The V_HH mixture also maintained excellent neutralization potency (IC_{50} between 0.3 and 0.6 nM) against the Wuhan-Hu-1 strain as well as Alpha and Lambda VOCs (Figure S1B). Notably, compared with the initial V_HHs, the neutralization potencies after booster were substantially increased to Beta, Delta, and SARS-CoV (IC_{50} of 0.58, 1.90, and 1.65 nM, respectively), corresponding to 6.0-, 2.3-, and 9.3-fold improvements (Figure S1B). Surprisingly, the booster was also associated with strong and broad binding against the RBDs from a full spectrum of sarbecoviruses (Figures 1A and 1B). The relative binding affinities (ELISA IC_{50}) for RBDs from clades 1a ($RBD_{SARS-CoV}$), 2 ($RBD_{RmYN02-CoV}$), and 3 ($RBD_{BM-4831-CoV}$) were 0.08, 0.09, and 0.14 nM, respectively,
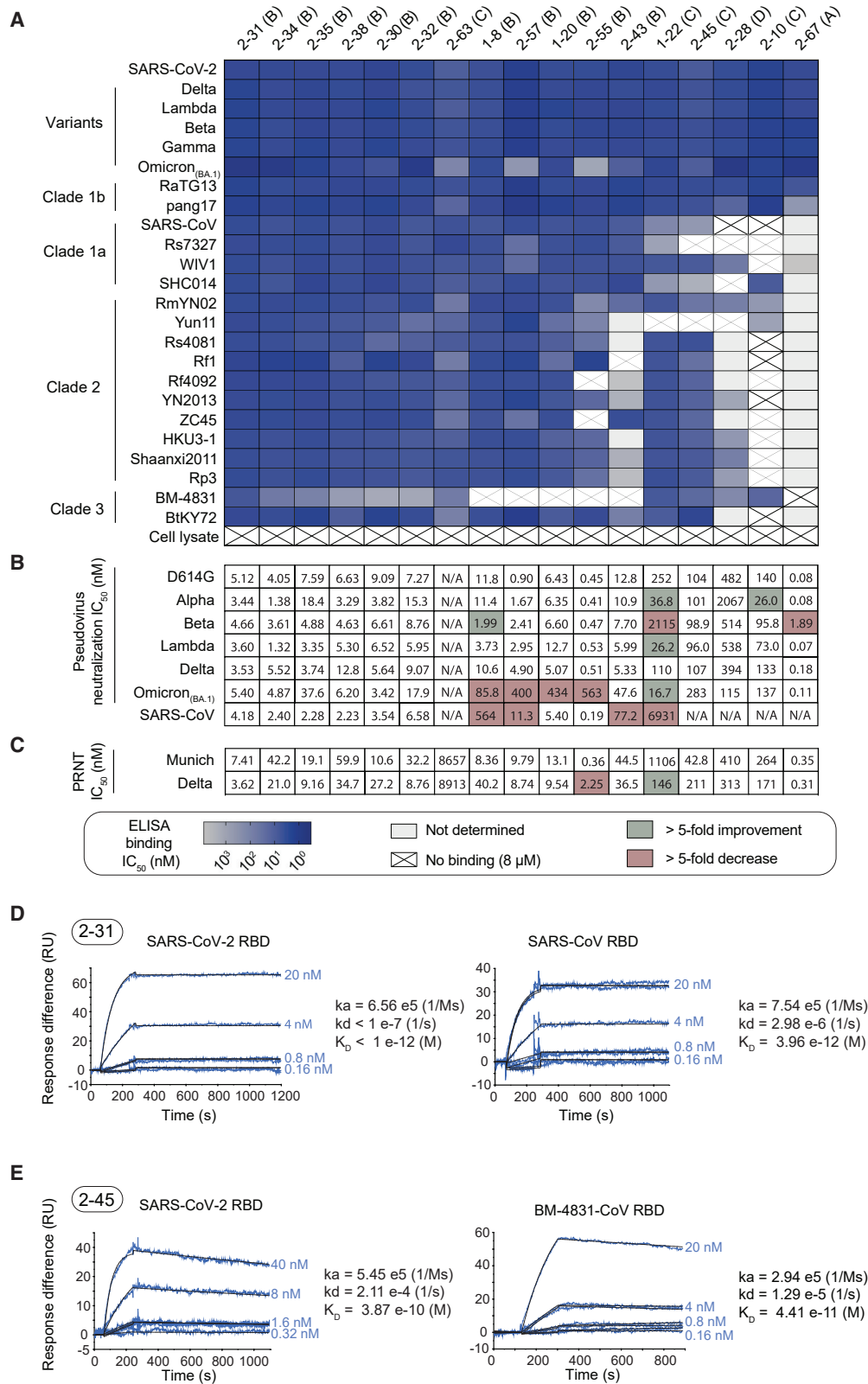
which correspond to 8.5-, 7.2-, and 8.6-fold improvements over the initial bleed (Figure S1A).

Next, we employed quantitative Nb proteomics (Xiang et al., 2021) to identify high-affinity psNbs that confer broad-spectrum activity in immunized sera (STAR Methods). This technology rapidly identified hundreds of distinct CDR3 families, from which a fraction of highly divergent Nbs were expressed and characterized. A total of 100 Nbs that interacted strongly with $RBD_{SARS-CoV-2}$ (clade 1b) were confirmed to cross-react with other sarbecovirus clades (Figure 1C and Table S1). Of these, 23%, 35%, and 42% were found to bind two, three, and all four sarbecovirus clades, respectively. Consistent with total polyclonal V_HH activity, psNbs isolated from the booster show broader pan-sarbecovirus activity than the initial bleed (Figure S2B). A substantial fraction (42%) was able to potently neutralize SARS-CoV-2 below 500 nM, with the best IC_{50} of 1.2 ng/mL (77 pM, psNb 2-67) and a median of 0.25 μg/mL (17 nM) (Table S1). Network analysis revealed that the psNbs are dominated by multiple clusters that span a large spectrum of physicochemical properties, including isoelectric point (pI) and hydropathy (Figures 1D and S2A). The three largest clusters are each composed of potent neutralizers (with the best IC_{50} of 6.8 ng/mL) that bind strongly to at least three sarbecovirus clades (Table S1). A smaller cluster (represented by psNbs 2-62 and 2-63) showed broad activity, yet only weakly neutralized SARS-CoV-2 in vitro (IC_{50} between 40 and 132 μg/mL; Table S1 and Figure S6). Other small clusters represented by psNbs 2-19, 2-16, 2-3, and 2-24 did not show neutralization at up to 37.5 μg/mL.

The psNbs were further classified by epitope binning using size-exclusion chromatography (SEC). psNb-$RBD_{SARS-CoV-2}$ complexes competed with high-affinity benchmark Nbs (Nb21, Nb105, and Nb36) that bind distinct and well-characterized epitopes (Sun et al., 2021; Figures S3A and S3B; STAR Methods). The psNbs fall into five groups: group A (3%) competes with Nb21 and targets RBS, group B (33%) with Nb105, group C (9%) with Nb36, and group D (17%) does not compete with any benchmark Nbs. Approximately one-third of psNbs (group E, 38%) bind strongly to RBDs based on ELISA, but do not neutralize pseudotyped SARS-CoV-2 efficiently. We selected a high-affinity psNb (2-47) from group E and confirmed its strong binding to the fully glycosylated but not the de-glycosylated RBD (Figure S3C; STAR Methods). It is possible that 2-47 can target an epitope encompassing the conserved, glycosylated RBD residue(s) (e.g., N343) (Walls et al., 2020). Together, these experiments suggest that a large cohort of high-affinity and divergent psNbs targeting multiple

---

Figure 1. Identification and characterization of psNbs

(A) Phylogenetic tree of 19 RBDs from all four clades of sarbecoviruses, constructed by the maximum likelihood method.

(B) The neutralization of polyclonal V_HHs from two immunization bleeds against pseudovirus of SARS-CoV-2, its variants, and SARS-CoV. Three biological replicates were performed and data are represented as the mean. Their ELISA IC_{50} against four RBD clades is also shown.

(C) Schematics for proteomic identification of psNbs from immunized sera.

(D) A map summarizing RBD binding and neutralization for 100 high-affinity psNbs. Nbs are represented by dots of various sizes and colors. Two Nbs are connected if their CDR sequence identity is >70%. Their neutralization potencies against pseudotyped SARS-CoV-2 (D614G) are represented by the size of dots. Breadth of sarbecovirus RBD binding is indicated by the filled gradient color (Table S1), and the SEC epitope groups (based on benchmark RBD Nbs) are colored on the outer circle (Figures S1, S2, and S3). The highest Nb concentrations used for binding and neutralization were 8 and 2.5 μM, respectively. The psNbs in bold were selected for downstream characterizations. psNbs isolated from the initial and booster bleed are denoted as 1- and 2-, respectively. See also Figures S1, S2, and S3 and Tables S1 and S6.

A

B

Pseudovirus neutralization IC$_{50}$ (nM)

	2-31 (B)	2-34 (B)	2-35 (B)	2-38 (B)	2-30 (B)	2-32 (B)	2-63 (C)	1-8 (B)	2-57 (B)	1-20 (B)	2-55 (B)	2-43 (B)	1-22 (C)	2-45 (C)	2-28 (D)	2-10 (C)	2-67 (A)
D614G	5.12	4.05	7.59	6.63	9.09	7.27	N/A	11.8	0.90	6.43	0.45	12.8	252	104	482	140	0.08
Alpha	3.44	1.38	18.4	3.29	3.82	15.3	N/A	11.4	1.67	6.35	0.41	10.9	36.8	101	2067	26.0	0.08
Beta	4.66	3.61	4.88	4.63	6.61	8.76	N/A	1.99	2.41	6.60	0.47	7.70	2115	98.9	514	95.8	1.89
Lambda	3.60	1.32	3.35	5.30	6.52	5.95	N/A	3.73	2.95	12.7	0.53	5.99	26.2	96.0	538	73.0	0.07
Delta	3.53	5.52	3.74	12.8	5.64	9.07	N/A	10.6	4.90	5.07	0.51	5.33	110	107	394	133	0.18
Omicron$_{(BA.1)}$	5.40	4.87	37.6	6.20	3.42	17.9	N/A	85.8	400	434	563	47.6	16.7	283	115	137	0.11
SARS-CoV	4.18	2.40	2.28	2.23	3.54	6.58	N/A	564	11.3	5.40	0.19	77.2	6931	N/A	N/A	N/A	N/A

C

PRNT IC$_{50}$ (nM)

	2-31	2-34	2-35	2-38	2-30	2-32	2-63	1-8	2-57	1-20	2-55	2-43	1-22	2-45	2-28	2-10	2-67
Munich	7.41	42.2	19.1	59.9	10.6	32.2	8657	8.36	9.79	13.1	0.36	44.5	1106	42.8	410	264	0.35
Delta	3.62	21.0	9.16	34.7	27.2	8.76	8913	40.2	8.74	9.54	2.25	36.5	146	211	313	171	0.31

Legend:
- ELISA binding IC$_{50}$ (nM): 10^3 10^2 10^1 10^0
- Not determined
- No binding (8 μM)
- > 5-fold improvement
- > 5-fold decrease

D

(2-31)

SARS-CoV-2 RBD
ka = 6.56 e5 (1/Ms)
kd < 1 e-7 (1/s)
K$_D$ < 1 e-12 (M)

SARS-CoV RBD
ka = 7.54 e5 (1/Ms)
kd = 2.98 e-6 (1/s)
K$_D$ = 3.96 e-12 (M)

E

(2-45)

SARS-CoV-2 RBD
ka = 5.45 e5 (1/Ms)
kd = 2.11 e-4 (1/s)
K$_D$ = 3.87 e-10 (M)

BM-4831-CoV RBD
ka = 2.94 e5 (1/Ms)
kd = 1.29 e-5 (1/s)
K$_D$ = 4.41 e-11 (M)

(legend on next page)

dominant RBD epitopes contributes to the broad-spectrum serologic activities.

Seventeen psNbs spanning four SEC groups (A–D) were tested for binding to RBDs of five SARS-CoV-2 variants, including the fast-spreading Omicron, and another 18 different sarbecovirus RBDs. These psNbs bind strongly to all variants that were evaluated. Sixteen of the 17 psNbs bind to all four clades (Figure 2A). Interestingly, seven psNbs (such as 2-31 and 2-45) have exceptionally broad activities and bind strongly to all 24 RBDs with a median ELISA IC_{50} of 3 nM (Figures 2A and S4 and Table S1). Two representative psNbs were measured for binding kinetics to all four clades by SPR. The K_D of 2-31 for $RBD_{SARS-CoV-2}$ (clade 1b), $RBD_{SARS-CoV}$ (clade 1a), $RBD_{RmYN02-CoV}$ (clade 2), and $RBD_{BM-4831-CoV}$ (clade 3) are <1 pM, 3.96 pM, 0.59 nM, and 3.60 nM, respectively (Figures 2D, S7A, and S7B). The binding of 2-45 is equally strong for clades 1b, 2, and 3 (0.39 nM, 1.4 nM, and 44 pM, respectively) and more moderate for clade 1a (304 nM) (Figures 2E, S7C, and S7D). Of note, these psNbs are highly specific to sarbecoviruses and do not cross-react with a human whole-protein extract at high concentrations (up to 8 μM) (Figure 2A).

All but one of these 17 psNbs can potently inhibit SARS-CoV-2 and VOCs *in vitro*, based on a pseudovirus assay and plaque reduction neutralization test (PRNT) against the Munich strain and Delta VOC (Figures 2B, 2C, S5, and S6; STAR Methods). Group A Nb 2-67, which preferentially binds to clade 1b, is extremely potent for SARS-CoV-2 and VOCs, including Omicron, with a median neutralization potency of 1.4 ng/mL. Group C (1-22, 2-10, and 2-45) neutralizes VOCs at single-digit micrograms per milliliter but is less effective against SARS-CoV. psNb 2-63 (group D) has exceptional breadth, while the other group D psNb, 2-28, has limited breadth. They both weakly neutralize SARS-CoV-2 (IC_{50} 7–132 μg/mL). The remaining psNbs belong to group B and show comparably high potency against SARS-CoV. The median potency for SARS-CoV-2 and VOCs, including Omicron, is 86 ng/mL, with the most potent (2-55) at 7 ng/mL. Notably, psNbs are usually highly stable and can withstand aerosolization without compromising activity, as exemplified by 2-31 and 2-45 (Figures S7E–S7G; STAR Methods). To demonstrate the high bioengineering potential of psNbs, we developed a bispecific construct (PiN-31) by fusing these two potent and broad-spectrum psNbs, which cover two distinct epitopes based on SEC. Compared with the monomers, the potency of PiN-31 is improved by an order of magnitude to 0.4 nM based on the PRNT assay (Figure S7H).

Diversity, convergence, and evolution of broadly neutralizing psNbs

To understand the mechanisms of broad neutralization, we implemented cryo-EM to interrogate the structures of 11 psNbs in complex with the SARS-CoV-2 spike or RBD (Table S2). In addition, two atomic psNb:RBD structures were determined by X-ray crystallography (Table S3). Epitope clustering based on high-resolution structures revealed five primary, distinct, and conserved epitope classes in $RBD_{SARS-CoV-2}$ (Figure 3A). None of our psNbs (except for 2-57) overlap with key RBD mutations in variants, including Alpha, Beta, Delta, Lambda, Gamma, and Omicron, including its sublineages (Figures 3B and 3C), in contrast to most other Nbs that have been structurally characterized (Guttler et al., 2021; Huo et al., 2020, 2021; Koenig et al., 2021; Pymm et al., 2021; Wagner et al., 2021; Xu et al., 2021; Ye et al., 2021) (Figure S8). Over three-quarters of the solvent-exposed and highly conserved RBD residues (sequence identity >85%) are covered by psNbs (STAR Methods). Superposition onto the spike structure reveals that psNbs preferentially lock RBDs in the three-up conformation (Figure 3D). Despite having different epitopes and orientations, the small size of Nbs facilitates simultaneous binding of three copies to the spike trimer in distinct and highly symmetric configurations.

The class II psNbs are overrepresented in our collection. Phylogenetic analysis reveals that, while psNbs are diverse, those isolated from the booster converge more than the initial bleed (Figure 4A). Two subclasses within the class II (A and B) differ in epitopes and Nb binding orientation (Figures 4B and 4D). Nevertheless, II(A) and II(B) psNbs share a conserved hydrophobic core epitope (aa 377–386) (Figure 4C) containing two bulky hydrophobic residues (F377 and Y380), and this region is stabilized by a disulfide bond (C379–C432). The improved breadth in class II(B) psNbs, especially for Omicron and clade 3 $RBD_{BM-4831-CoV}$, lies in its ability to target an additional conserved region with peripheral charged residues (aa 412–415, 427–429). In contrast, subclass II(A) psNbs bind to a less conserved epitope that is composed of primarily hydrophobic residues (e.g., L368, A372, and Y508) (Figure 4C). Notably, A372 on SARS-CoV-2 (clade 1a) is substituted to S/T in other clades, forming a consensus glycosylation motif (^{370}NST/S^{372}) (Watanabe et al., 2020), which may explain the reduced neutralization potency of class II(A) psNbs versus class (B) psNbs against Omicron and SARS-CoV (Figures 2B and 4B).

Class II(B) psNbs comprise two large clusters possessing the best breadth and potency (Figure 1D). While the epitopes largely overlap in the complex structure, the molecular interactions vary substantially. For example, two related psNbs (2-38 and 1-21)

Figure 2. Binding and neutralization of 17 representative, diversified psNbs

(A) Heatmap summary of psNbs for binding to different RBDs by ELISA. The epitope group of psNbs according to SEC is labeled in parentheses. White with cross mark, no binding; silver, binding signals were detected at 8 μM, yet the IC_{50} has not been determined; blue shades, IC_{50} between 0.8 nM and 8 μM. Two biological replicates were performed for each Nb.

(B) Neutralization potency of psNbs against pseudotyped SARS-CoV-2, its variants, and SARS-CoV. N/A, no neutralization detected at the highest Nb concentration (2.5 μM). At least two biological replicates were performed for each Nb and data are represented as the mean.

(C) Neutralization potency against SARS-CoV-2 Munich strain and the Delta VOC by the PRNT assay. At least two biological replicates were performed for each Nb and data are represented as the mean.

(D) Binding kinetic measurements of 2-31 for the RBDs of SARS-CoV-2 and SARS-CoV by surface plasmon resonance (SPR).

(E) Binding kinetic measurements of 2-45 for the RBDs of SARS-CoV-2 and BM-4831-CoV. See also Figures S4, S5, S6, and S7 and Tables S1 and S6.
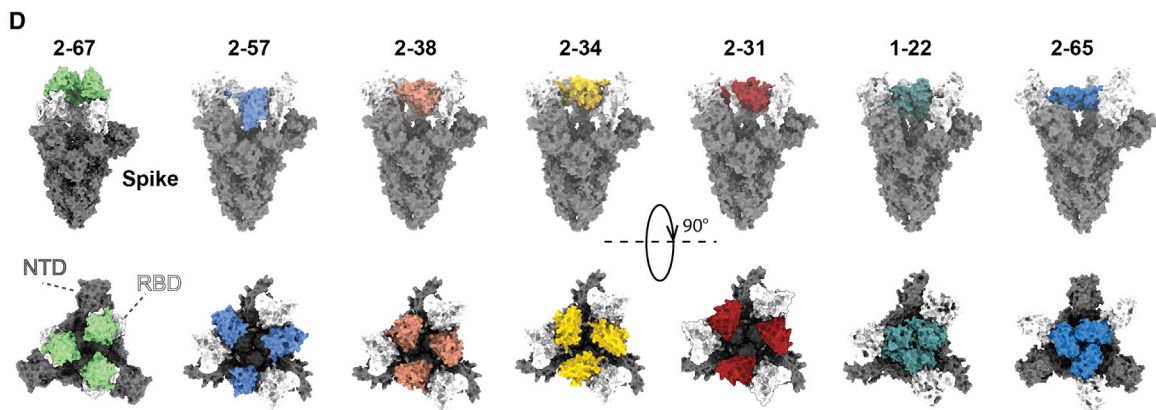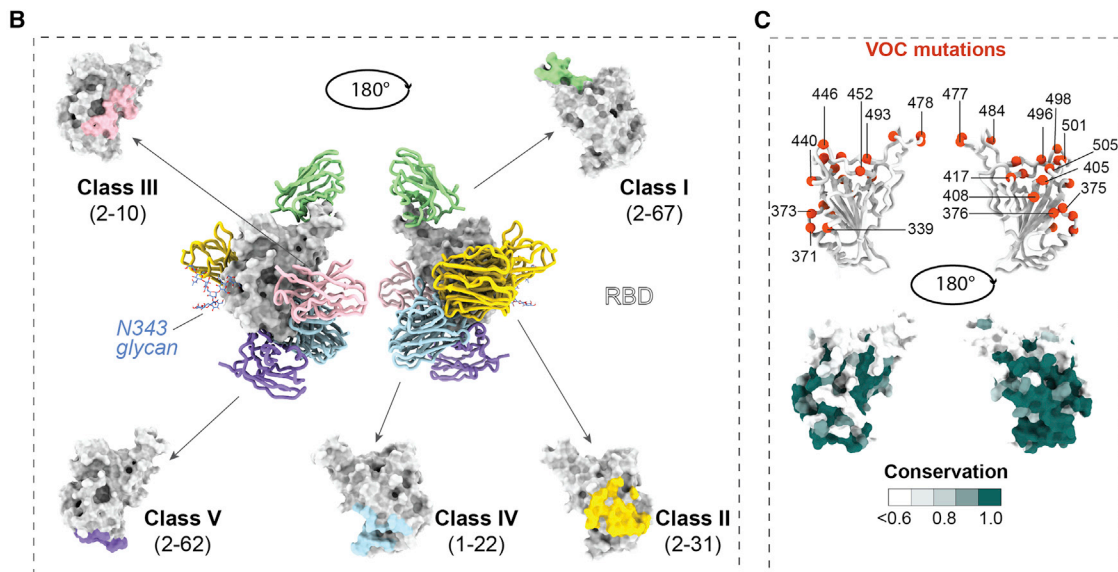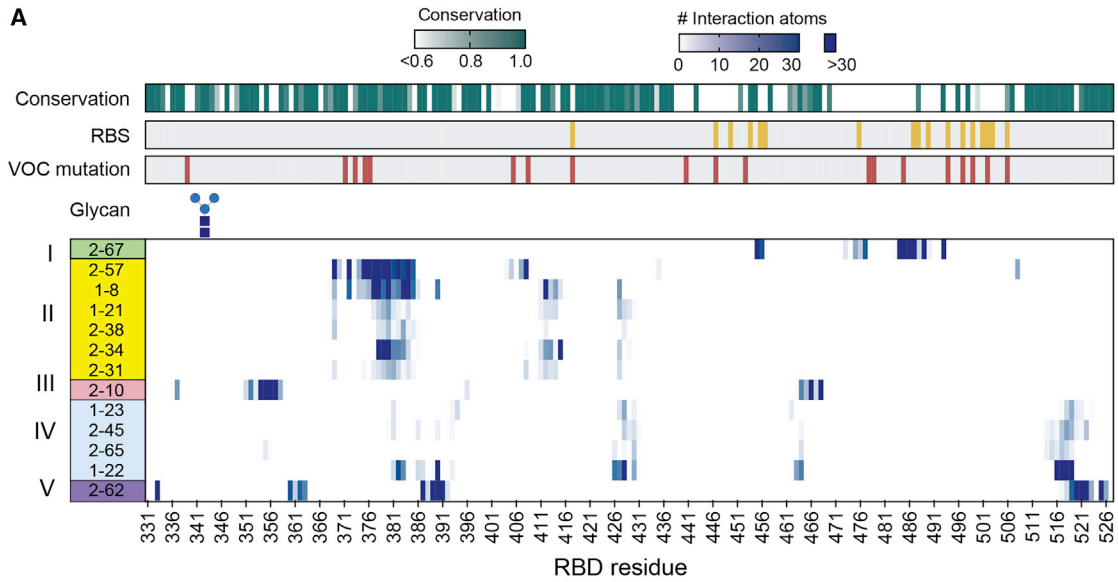
(legend on next page)

are characterized by a short CDR3 (13 aa) forming a β-strand hairpin conformation. Yet, psNb 2-38 is an all-clade binder, whereas 1-21 binds strongly to all but RBD$_{BM-4831-CoV}$ (clade 3). The difference in binding is likely due to the K378Q substitution in the RBD, which disrupts a critical salt bridge between D110 (1-21) and K378 (RBD$_{SARS-CoV-2}$) (Figures 4E, S9B, S12A, and S12B). psNbs 2-34 and 2-31 (from the other dominant cluster) bind all 24 RBDs strongly with potent antiviral activities. The interactions are predominantly mediated by a long CDR3 loop (18 aa) with a small helix. These Nbs form hydrophobic interactions and also bind strongly to conserved charged residues (such as D427 and R408) through electrostatic interactions (Figures 4F, S9A, S12C, and S12D).

The class II(A) psNb (2-57) shares high sequence similarity with Nb105 (isolated from the initial bleed). The major difference lies in their CDR3 heads. Here, a small CDR3 loop of [109]DLF[111] in Nb105 is substituted by [109]QST[111] in 2-57, which inserts into two conserved pockets (RBD residues F377, Y369, F374 and residues S375, T376, Y508, V407), forming extensive hydrophobic interactions with the RBD (Figures 4G, S10, S11, S12E, and S12F). This substitution allows psNb 2-57 to tolerate sequence variation better, exhibiting over 100-fold higher affinities for clade 2 RBDs (Table S1).

Class I psNbs that bind the RBS are extremely potent yet rare (~3%). The structure of the ultrapotent 2-67 was resolved by cryo-EM in complex with the RBD (Figure S13). Superposition of 2-67:RBD and hACE2:RBD (PDB: 6M0J) (Lan et al., 2020) structures revealed major clashes between all three Nb framework regions and two CDRs (2 and 3) with hACE2 (aa 26–37, 66–87, 91–109, 187–194) (Figure 5A). psNb 2-67 targets the protruding RBD ridge (aa 472–490) (Figures 5B and S15A). Binding energy analysis (STAR Methods) reveals that, compared with other RBS Nbs (Guttler et al., 2021; Huo et al., 2020, 2021; Koenig et al., 2021; Pymm et al., 2021; Wagner et al., 2021; Xu et al., 2021; Ye et al., 2021), the RBD binding epitope of 2-67 contains a minimal number of critical VOC residues (Figure 5C and Table S5). Here, 2-67 utilizes all CDRs to form extensive networks of hydrophobic and non-polar interactions with two critical RBD residues that are not present as VOC mutations (F486 and Y489) and, therefore, can achieve ultrahigh affinity for SARS-CoV-2 and retain strong binding and neutralization against the variants (Figure 5D). Moreover, 2-67 can outcompete ultra-high-affinity Nb21 for RBS binding, thereby further corroborating the ultrahigh affinity of this interaction (Figure S14A) (Xiang et al., 2020). Interestingly, quantitative mass spectrometric analysis reveals that ultrapotent RBS binders (e.g., Nbs 20 and 21) identified from the initial bleed were absent in the

booster, implying that they are sourced from short-lived plasma cells (Akkaya et al., 2020) (Figure S14B).

The class III psNb (2-10) can destabilize the spike *in vitro*, as we observed previously (Sun et al., 2021). However, the structure can be resolved by reconstituting an RBD:4 Nb complex by cryo-EM (STAR Methods, Figure S13). psNb 2-10 targets a rare non-RBS epitope that partially overlaps with that of Nb17 (Figure 5E) isolated from the initial bleed that is partially effective against variants (Sun et al., 2021). Class III psNbs bind strongly to RBD variants and clade 1b and show selectivity within other clades. Compared with Nb17, with limited breadth, the improved breadth of class III psNbs is contributed by a recognition motif that shifts (from aa 356–357 to aa 449–450, 481-484, and 490–494) toward a smaller and more conserved epitope (Figures 5F and S15B).

Four Class IV psNbs (1-22, 1-23, 2-65, and 2-45) were resolved by cryo-EM. Their binding involves a plethora of molecular contacts that are dependent upon distinct scaffold orientations, different CDR combinations, and sequence-specific bonding networks. Class IV shares a highly conserved and cryptic epitope that is accessible only in the RBD-up conformation (Figures 3A–3C and 5G). The epitope is characterized by charged and hydrophobic residues (D427/D428, T430, F464, [516]ELLH[519]) forming a cavity (Figure 5G). CDR3s of class IV adopt a "hairpin" conformation that inserts into the RBD cavity, forming extensive hydrophobic and polar interactions. psNbs 1-22 and 1-23 are all-clade binders that recognize multiple other conserved RBD residues (L390, P426, and P463 for 1-22 and Y369 for 1-23) through hydrophobic interactions (Figures S15C and S15D). psNb 2-65 shows selectivity toward clade 1b and clade 3, likely due to a salt bridge between D124 (CDR3) and the semi-conserved H519 on RBDs (Figure S15E). Notably, the class IV epitope partially overlaps with a recently discovered broadly neutralizing antibody, S2H97 (Starr et al., 2021), and targets RBD from a distinct angle (Figure S16). Compared with S2H97, which depends on bulky aromatic side chains (W, F, and Y) for interaction, the binding of 1-22 is primarily mediated through a combination of hydrophobic, non-aromatic (L, I, and V), and basic (R and H) residues. Facilitated by a distinct orientation, class V psNb 2-62 (which shares high CDR similarity with 2-63) targets RBD through a conserved epitope (T333, L387, [389]DLC[391], C525, L517, and P521) completely buried in the spike and a region that marginally overlaps with the binding motif of class IV psNbs (i.e., L517 and H519) (Figures 5H and 5I). While 2-62 binds tightly to the RBD, it does not bind the pre-fusion spike and is therefore a poor neutralizer of the virus (Figure S6).

Figure 3. Summary of broadly neutralizing RBD epitopes and spike conformations

(A) Clustering analysis of psNb epitopes. RBS residues are in yellow. The RBD glycosylation site (N343) is indicated. Sarbecovirus sequence conservation is shown in a green gradient. The numbers of psNb:RBD interaction atoms per epitope residue are shown in blue shades.

(B) Structural representations of the five classes of psNbs in complex with RBD and the corresponding epitopes. Light green, class I (2-67); gold, class II (2-31); pink, class III (2-10); light blue, class IV (1-22); and purple, class V (2-62). VOC residues are in red. RBD glycosylation (N343) is in cornflower blue.

(C) The same set of views is used for comparison between psNb epitopes, VOC mutation sites, and RBD conservation. Top: RBDs are shown in ribbon representation, and VOC mutations are shown in red spheres. Bottom: RBDs are shown in surface representation; the surface is colored based on RBD sequence conservation. All the annotated mutations are identified in the Omicron subvariants.

(D) Structural diversity of psNbs in complex with the SARS-CoV-2 pre-fusion spike glycoprotein (by cryo-EM). RBDs are shown in white and non-RBD regions of spike in gray. See also Figure S8 and Tables S2 and S3.
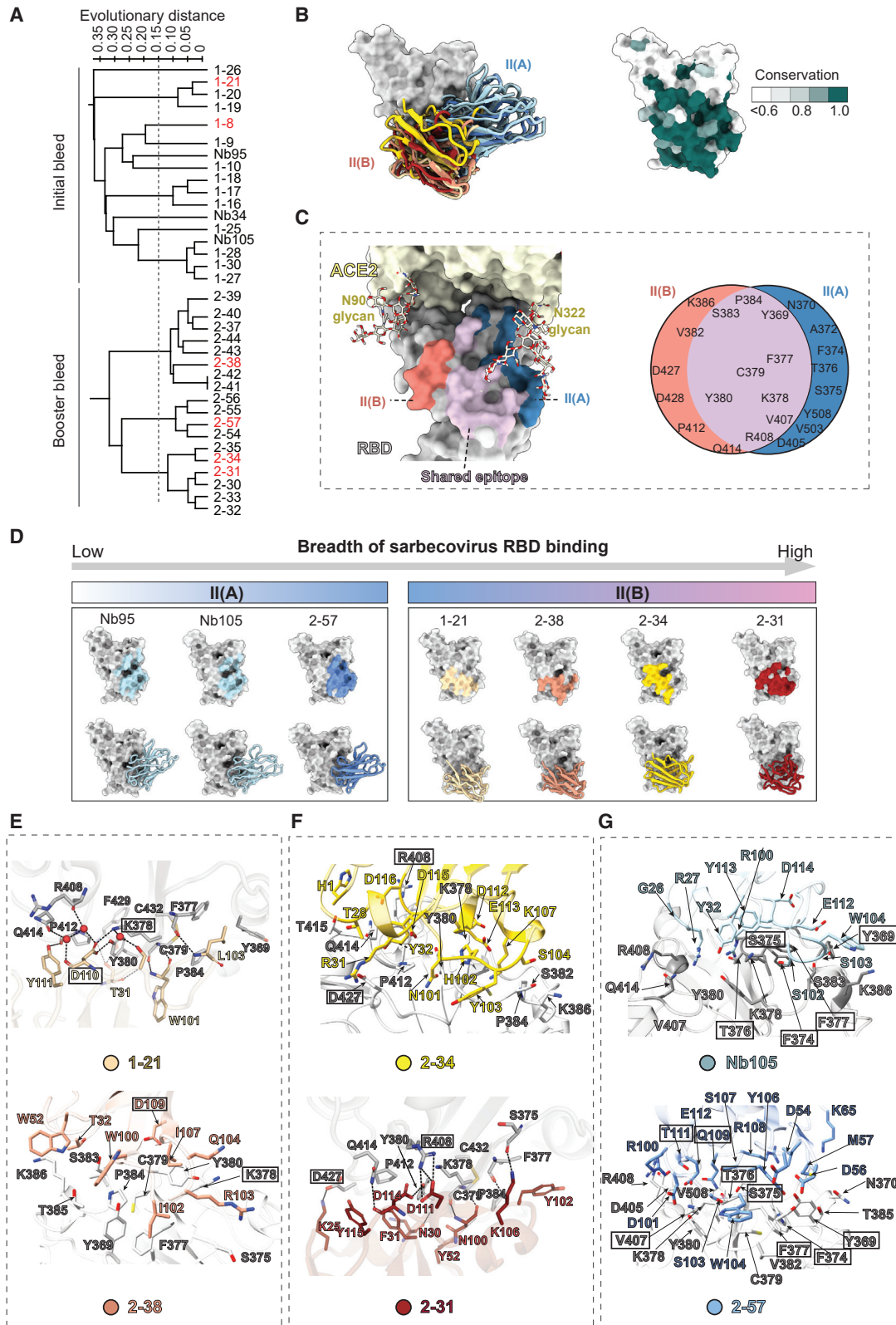
(legend on next page)

Mechanisms of broad neutralization by psNbs

Our comprehensive investigation provides direct evidence that, with successive immunizations, antibodies emerged in the serum that concurrently and almost exhaustively targeted diverse and conserved physicochemical and geometric sites on the RBD. We observed that ultra-high-affinity Nbs (i.e., sub-nanomolar) exhibit neutralization potencies that correlate inversely, almost perfectly, with the distance of their epitopes from the RBS (Figures 6A and 6B; STAR Methods). Ultrapotent class I psNbs neutralize the virus at single-digit nanograms per milliliter by binding to the RBS to block hACE2 binding (Figure S17). Class II psNbs can still efficiently neutralize the virus (i.e., single-digit nanograms per milliliter) primarily by sterically interfering with the receptor binding. In particular, binding to the RBD can clash with the glycan moiety at N322 of hACE2, especially bulky complex-type glycans (Mehdipour and Hummer, 2021) (Figure S17). Classes III, IV, and V possess substantially weaker potencies. Their epitopes are distant from the RBS and do not compete with hACE2 in vitro.

To better understand the broad activities of psNbs, we also expressed a set of high-affinity RBD Nbs that have been previously characterized (Guttler et al., 2021; Huo et al., 2020, 2021; Koenig et al., 2021; Pymm et al., 2021; Wagner et al., 2021; Xu et al., 2021; Ye et al., 2021) and evaluated cross-reactivity by ELISA (Table S4; STAR Methods). Nbs fall into two groups based on RBS occupancy. Overall, their cross-reactivities positively correlate with epitope sequence conservation (Figure 6C). psNbs that do not bind the RBS can be separated based on high epitope conservation (>0.85) (Figure 6D). Critical mutations from the variants are predominantly located on the RBS but also recently on a small patch of relatively conserved residues (e.g., aa 371, 373, and 375) in Omicron (B.1.1.529). In addition, the virus can mutate on A372S/T to acquire an N-linked glycan (N370) similar to other sarbecoviruses to blunt the host antibody response (Nabel et al., 2021). While most Nbs and human IgGs directly interact with these residues, psNbs are barely affected (Figures 2A, 2B, and S5). Mutations on these highly conserved epitopes can cause RBD instability, reducing viral fitness (Starr et al., 2020) (Figure 6E).

Compared with RBS Nbs that bind to concave epitopes, psNbs generally target smaller (Figure 6H) and flat (classes II, III, and V) or convex (classes I and IV) regions (Figure 6F). psNb epitopes are also more flexible based on average root-mean-square fluctuation (RMSF) for epitope residues (Figure 6G and Table S5; STAR Methods). Together, these properties may render high-affinity binding particularly challenging. Consis-tently, ScanNet, a geometric deep-learning model, reveals that RBS epitopes are predominantly targeted by Nbs (and IgG antibodies), while the psNb epitopes are hardly recognized (Figure S19). Moreover, compared with non-psNbs, psNbs utilize almost exclusively hypervariable CDR loops (Figure S18). Conceivably, extensive affinity maturation is required to bind these conserved yet difficult-to-bind epitopes.

DISCUSSION

SARS-CoV-2 continues to evolve, producing variants with high transmissibility and potential to evade host immunity (Harvey et al., 2021; Karim and Karim, 2021). Most updated evidence indicates that infection or vaccination by boosting can improve the host antibody response against SARS-CoV-2 variants (Callaway, 2021; Cho et al., 2021; Schmidt et al., 2021; Stamatatos et al., 2021; Wang et al., 2021). Here we discovered that successive immunization of a camelid by a recombinant RBD can enhance the development of superimmunity. Integrative proteomics facilitated rapid identification of a large repertoire of high-affinity V$_H$H antibodies (Nbs) from immunized sera against SARS-CoV-2 VOCs and the full spectrum of the sarbecovirus family. Cryo-EM and X-ray crystallography were able to systematically map broadly neutralizing epitopes and interactions, providing insights into the structural basis and evolution of serologic activities. Our data support the notion that the RBD structure alone can drive this impressive level of evolution, reshaping the immunogenic landscape toward conserved epitopes. The initial immune response predominantly targets the RBS due to its favorable properties for protein-protein interactions (both host receptor and antibody binding). High-affinity antibodies can evolve to saturate this critical region with extremely high neutralization potency. However, broadly neutralizing antibodies will emerge (with unprecedented diversity) and can continuously develop improved affinity to target conserved epitopes, which provide resistance to antigenic drift. Their neutralization potencies vary substantially yet are strongly and negatively correlated with the distance of epitopes from the RBS center for viral entry and effective host immunity. Together, our findings inform the development of safe and broadly protective countermeasures such as vaccines and therapeutics.

Preference for non-conserved epitopes is also observed in other viral antigen structures (Figure S20). We suggest that evolutionary conservation imposes constraints on spatiochemical surface properties, which in turn constrains the immunogenicity of and access to epitopes, as hinted by an overall negative

---

Figure 4. Structural diversity, convergence, and evolution of class II psNbs

(A) Phylogenetic analysis of psNbs from SEC group B. psNbs with structures determined in this study are in red. Scale of the evolutionary distance, 0–0.35.

(B) Left: superposition of class II psNbs reveals two subclasses, II(A) and II(B). Right: surface representation of RBD showing sequence conservation.

(C) Overlap between II(A) and II(B) epitopes. Purple, shared epitope; blue, non-overlapping epitope of II(A); salmon, non-overlapping epitope of II(B); light yellow, hACE2 with modeled glycans (N90 and N322).

(D) Structural overview of class II psNbs in complex with RBD and their epitopes. Light blue, Nb95 and Nb105; cornflower blue, 2-57; beige, 121; salmon, 238; gold, 2-34; dark red, 2-31.

(E–G) Interactions of epitope II psNbs in complex with the spike or RBD. Key residues involved in the RBD:psNb interfaces are shown as sticks. Hydrogen bonds or salt bridges are indicated with dashed lines. Water molecules mediating interactions between 1-21 and SARS-CoV-2 RBD are shown in red spheres. psNb 1-21 is in Navajo white; 2-38 in dark salmon; 2-34 in gold; 2-31 in reddish brown; Nb105 in light blue; 2-57 in cornflower blue; and RBD in light gray. Key residues contributing to the differences in activities are boxed. See also Figures S9, S10, S11, and S12.
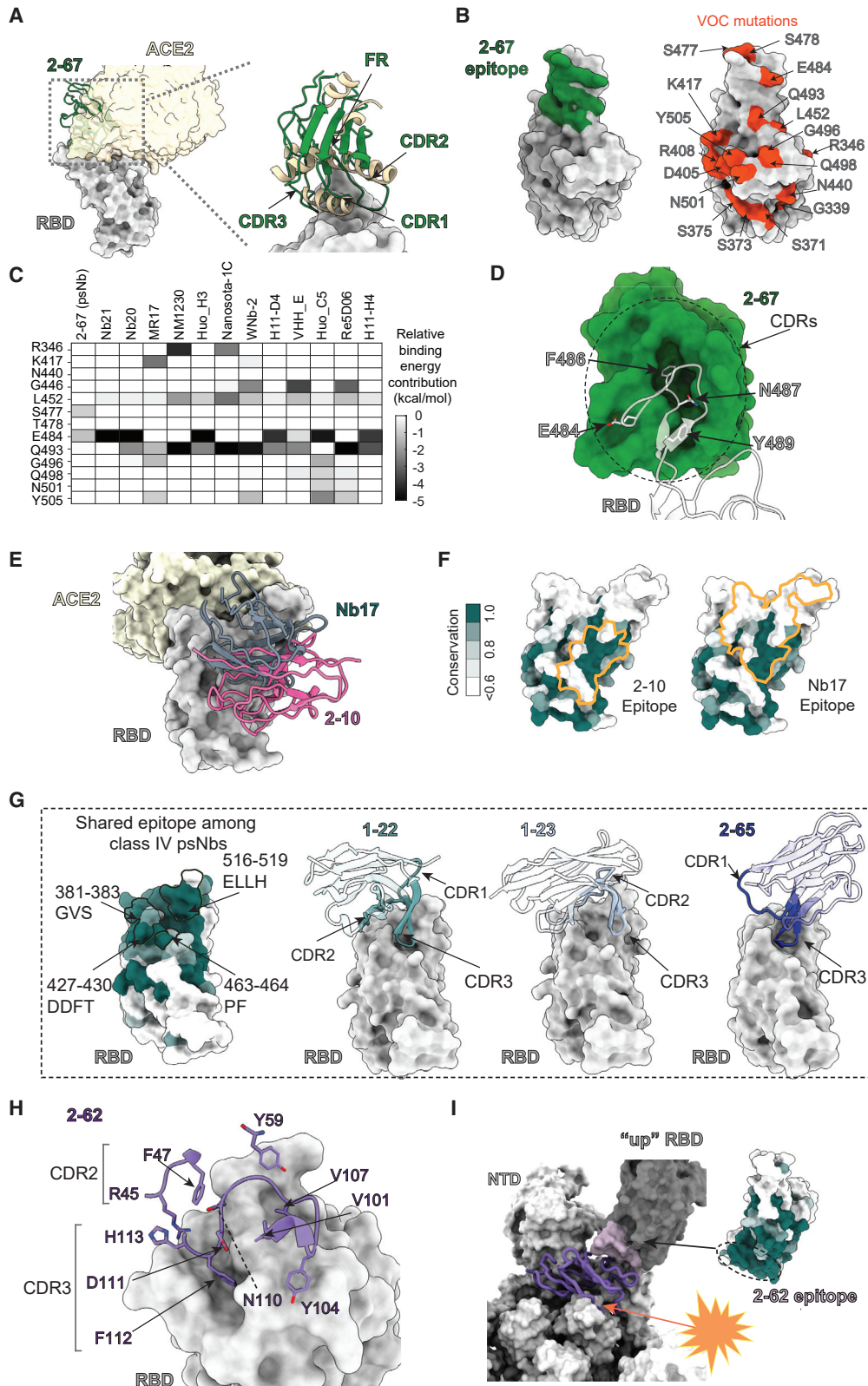
(legend on next page)

correlation between conservation and predicted epitope propensity (Figure S21). However, antibody repertoires are dynamic and can evolve toward conserved epitopes. In addition to COVID-19 superimmunity, potent broadly neutralizing antibodies have also been isolated from HIV elite controllers, although they usually take years to evolve (Sok and Burton, 2018).

Our highly selected psNbs can bind strongly and specifically to all sarbecoviruses for potent neutralization with the best median antiviral potencies at single-digit nanograms per milliliter, which is extremely rare for cross-reactive antibodies (Walker and Burton, 2018). Multivalent constructs (such as PiN-31) that target distinct and conserved epitopes and their cocktails may provide comprehensive coverage against future SARS-CoV-2 antigenic drift and future sarbecovirus challenges. The low production costs and marked stability of Nbs (Koenig et al., 2021; Mast et al., 2021; Muyldermans, 2013; Pymm et al., 2021; Schoof et al., 2020) and other miniproteins (Cao et al., 2020) allow for more equitable and efficient distribution globally, particularly for developing countries and regions that are vulnerable to viral spillovers. Combined with their small size (high effective dose and bioavailability) and flexible administration routes that protect both upper and lower respiratory tracts to limit airborne transmission (Nambulli et al., 2021), ultrapotent and inhalable psNbs are highly complementary to vaccines, small-molecule drugs, and monoclonal antibody therapeutics (Cully, 2021; Liu et al., 2020a). The prospects of winning the race against future outbreaks will rely on the fast development and equitable distribution of an arsenal of broadly protective, cost-effective, and convenient technologies.

Limitations of the study
A main focus of this study is to understand the superimmunity given by broad-spectrum camelid single-chain antibodies. We have characterized a large number of psNbs and determined 13 high-resolution structures of highly diverse psNbs in complex with the SARS-CoV-2 spike or RBD, which provide insights into the mechanisms of their pan-sarbecovirus activities. However, it is worth noting that despite these efforts, our structural information remains limited for fully appreciating this remarkable antibody maturation process, which seems to be driven by antigenic structures, and its implications in the race between host immunity and viral evolution. While we found that extensive RBD inoculation can drive the development of broad-spectrum serologic activities in the camelid, it would be interesting to compare our

observation with other strategies, such as immunization by mosaic nanoparticles using heterotypic RBDs for display (Cohen et al., 2021). Finally, for future work, it would be of interest to design a large panel of psNb polymers with avid binding to sarbecoviruses and thoroughly evaluate their pre-clinical implications in both rodent and primate models, under different sarbecovirus challenges, and to evaluate delivery strategies, including aerosolization, for future clinical trials.

STAR★METHODS

Detailed methods are provided in the online version of this paper and include the following:

- KEY RESOURCES TABLE
- RESOURCE AVAILABILITY
  - Lead contact
  - Materials availability
  - Data and code availability
- EXPERIMENTAL MODEL AND SUBJECT DETAILS
- METHOD DETAILS
  - Purification of recombinant sarbecovirus RBDs and SARS-CoV-2 spike
  - Successive camelid immunization with RBD and the proteomic identification of psNbs
  - Nb DNA synthesis and cloning
  - Purification of Nbs
  - ELISA (enzyme-linked immunosorbent assay)
  - Competitive ELISA with recombinant hACE2
  - psNb epitope analysis by competitive size exclusion chromatography (SEC)
  - Nb affinity measurement by SPR
  - Pseudotyped SARS-CoV-2 neutralization assay
  - SARS-CoV-2 Munich and Delta plaque reduction neutralization test (PRNT)
  - Biological safety
  - Aerosolization of PiN using a soft-mist inhaler
  - Cryo-electron microscopy data collection and image processing
  - Model building and refinement
  - Calculation for binding energy contribution
  - Crystallographic analysis of psNbs with RBD
  - RBD epitope analysis by ScanNet
  - Conservation and ScanNet analysis of viral antigens
  - RMSF calculation

Figure 5. Structural insights of four classes of psNbs
(A) Superposition of a class I psNb (2-67):RBD with hACE2 showing steric effects.
(B) The 2-67 epitope (green) and critical VOC mutations (red) on RBD.
(C) Heatmap of relative binding energy contribution of Nbs per epitope residue that overlaps with critical mutations from VOCs. Nbs targeting RBSs with high-resolution structures from PDB were included in the analysis.
(D) Surface representation showing all CDRs of 2-67 with RBD. Green, 2-67; white, RBD.
(E) Superposition of a class III psNb (2-10) and a non-psNb (Nb17).
(F) The conservation map of RBD and the epitopes of a class III psNb (2-10) and Nb17.
(G) Shared epitopes and binding of three class IV psNbs (1-22, 1-23, and 2-65) to the RBD. Shared epitope residues are highlighted on the RBD structure with sequences labeled on the side.
(H) Binding of a class V psNb (2-62) with the RBD. Interacting CDR residues are labeled.
(I) Superposition of 2-62 from the 2-62:RBD structure showing the clash between 2-62 and the spike in the all-RBD-up conformation. NTD, N-terminal domain. Representation showing the 2-62 epitope is conserved but not accessible on the spike. See also Figures S13, S14, S15, and S16.
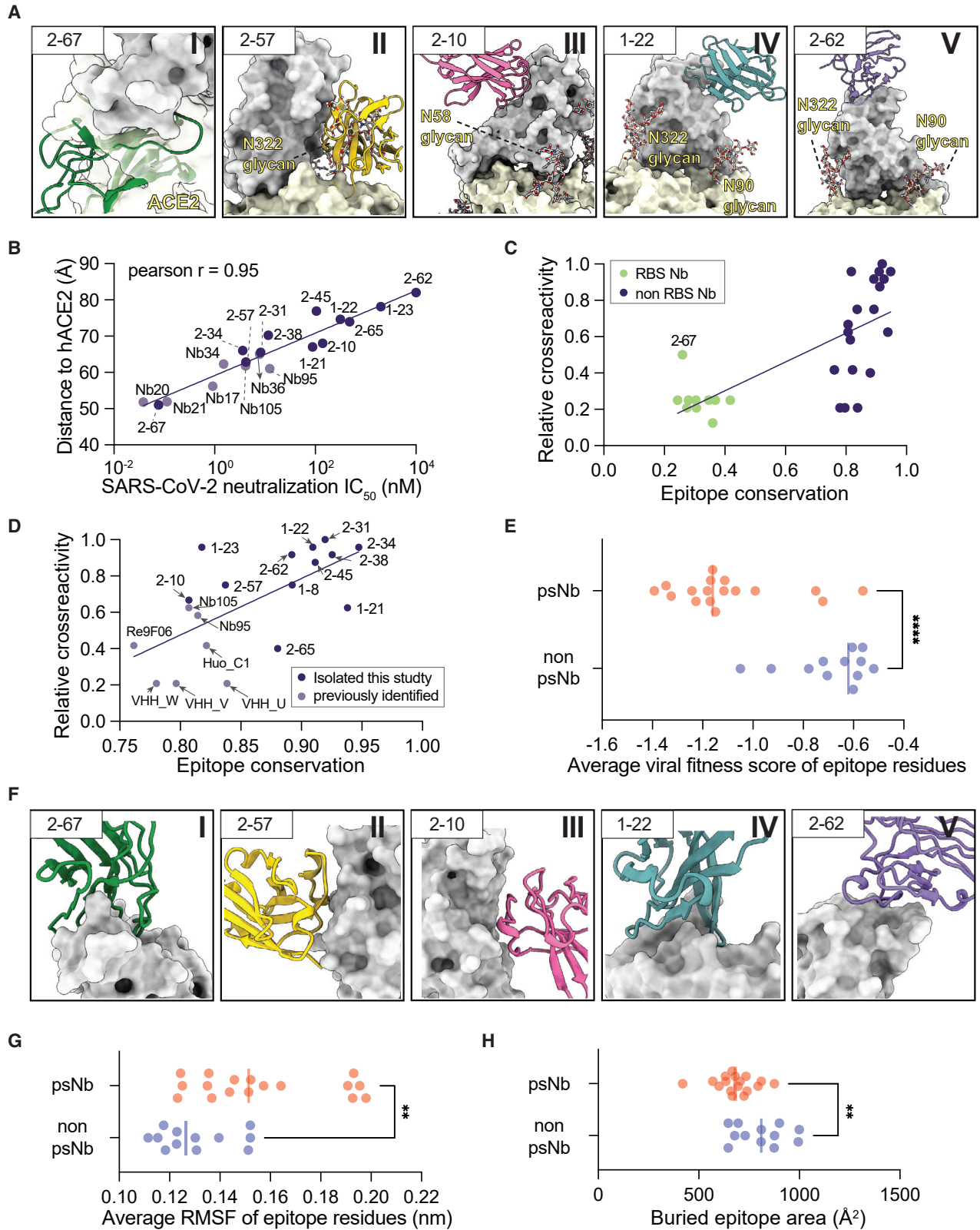
(legend on next page)

○ Phylogenetic analysis
○ Sarbecovirus RBD conservation
○ psNb epitope clustermap
○ Measurement of buried surface area (BSA)
○ Distance between Nb epitope and receptor binding sites
○ Viral fitness score of epitope residues
○ Glycosylation modeling
● QUANTIFICATION AND STATISTICAL ANALYSIS

SUPPLEMENTAL INFORMATION

Supplemental information can be found online at https://doi.org/10.1016/j.celrep.2022.111004.

AUTHOR CONTRIBUTIONS

Y.S. conceived the study. Y.X. identified and characterized Nbs. Z.S. developed scripts and analyzed structures. W.H. and D.J.T. solved cryo-EM structures. H.L. and I.A.W. determined and analyzed X-ray crystallographic structures. J.T. and D.S. analyzed viral antigenicity. S.N. and P.W.D. performed the PRNT assay. Y.S. and Y.X. drafted the manuscript with substantial input from I.A.W., W.H., Z.S., D.S., H.L., and D.J.T. All authors reviewed the manuscript. We thank D.S. Reed (University of Pittsburgh) and N.A. Crossland (Boston University) for technical assistance.

REFERENCES

Afonine, P.V., Poon, B.K., Read, R.J., Sobolev, O.V., Terwilliger, T.C., Urzhumtsev, A., and Adams, P.D. (2018). Real-space refinement in PHENIX for cryo-EM and crystallography. Acta Crystallogr. D Struct. Biol. 74, 531–544. https://doi.org/10.1107/S2059798318006551.

Akkaya, M., Kwak, K., and Pierce, S.K. (2020). B cell memory: building two walls of protection against pathogens. Nat. Rev. Immunol. 20, 229–238. https://doi.org/10.1038/s41577-019-0244-2.

Aria, H., Mahmoodi, F., Ghaheh, H.S., Faranak, M., Zare, H., Heiat, M., and Bakherad, H. (2022). Outlook of therapeutic and diagnostic competency of nanobodies against SARS-CoV-2: a systematic review. Anal. Biochem. 640, 114546. https://doi.org/10.1016/j.ab.2022.114546.

Ashkenazy, H., Abadi, S., Martz, E., Chay, O., Mayrose, I., Pupko, T., and Ben-Tal, N. (2016). ConSurf 2016: an improved methodology to estimate and visualize evolutionary conservation in macromolecules. Nucleic Acids Res. 44, W344–W350. https://doi.org/10.1093/nar/gkw408.

Boni, M.F., Lemey, P., Jiang, X., Lam, T.T.Y., Perry, B.W., Castoe, T.A., Rambaut, A., and Robertson, D.L. (2020). Evolutionary origins of the SARS-CoV-2 sarbecovirus lineage responsible for the COVID-19 pandemic. Nat. Microbiol. 5, 1408–1417. https://doi.org/10.1038/s41564-020-0771-4.

Callaway, E. (2021). COVID super-immunity: one of the pandemic's great puzzles. Nature 598, 393–394. https://doi.org/10.1038/d41586-021-02795-x.

Cao, L., Goreshnik, I., Coventry, B., Case, J.B., Miller, L., Kozodoy, L., Chen, R.E., Carter, L., Walls, A.C., Park, Y.J., et al. (2020). De novo design of picomolar SARS-CoV-2 miniprotein inhibitors. Science 370, 426–431. https://doi.org/10.1126/science.abd9909.

Case, D.A., Cheatham, T.E., 3rd, Darden, T., Gohlke, H., Luo, R., Merz, K.M., Jr., Onufriev, A., Simmerling, C., Wang, B., and Woods, R.J. (2005). The Amber biomolecular simulation programs. J. Comput. Chem. 26, 1668–1688. https://doi.org/10.1002/jcc.20290.

Cho, A., Muecksch, F., Schaefer-Babajew, D., Wang, Z., Finkin, S., Gaebler, C., Ramos, V., Cipolla, M., Mendoza, P., Agudelo, M., et al. (2021). Anti-SARS-CoV-2 receptor-binding domain antibody evolution after mRNA vaccination. Nature 600, 517–522. https://doi.org/10.1038/s41586-021-04060-7.

Cohen, A.A., Gnanapragasam, P.N.P., Lee, Y.E., Hoffman, P.R., Ou, S., Kakutani, L.M., Keeffe, J.R., Wu, H.J., Howarth, M., West, A.P., et al. (2021). Mosaic

---

Figure 6. Mechanisms of broad neutralization

(A) Superposition of different psNb classes with RBD and hACE2. Key hACE2 glycosylation sites are shown (N90 and N322).

(B) Correlation between neutralization potency and the distance between the Nb epitope and the RBS. The distance is calculated based on centroids of the Nb epitope and hACE2 epitope.

(C and D) Correlation between cross-reactivity and epitope conservation for (C) all RBD Nbs and (D) non-RBS Nbs. The relative cross-reactivity is represented by the normalized ELISA binding of four sarbecovirus RBD clades.

(E) Comparison of the averaged viral fitness score of RBD epitope residues between psNbs and non-psNbs. The fitness score (Starr et al., 2020) is obtained by evaluating the mutational effects on RBD expression level. Negative values correspond to higher loss of fitness.

(F) Structures showing the geometric features of Nb:RBD interfaces for five classes of psNbs.

(G) Comparison of average root-mean-square fluctuation (RMSF) of epitope residues between psNbs and non-psNbs (Table S5).

(H) Comparison of buried surface area of epitope between psNbs and non-psNbs. For (E), (G), and (H), the data are expressed as scatterplots, and medians are shown as a solid line. The significant difference between two groups (n = 17 for psNb and n = 12 for non-psNb) was analyzed by Student's unpaired two-tailed t test. **$p \leq 0.01$; ****$p \leq 0.0001$. See also Figures S17 and S18 and Table S5.

nanoparticles elicit cross-reactive immune responses to zoonotic coronaviruses in mice. Science *371*, 735–741. https://doi.org/10.1126/science.abf6840.

Cully, M. (2021). A tale of two antiviral targets - and the COVID-19 drugs that bind them. Nat. Rev. Drug Discov. *21*, 3–5. https://doi.org/10.1038/d41573-021-00202-8.

Detalle, L., Stohr, T., Palomo, C., Piedra, P.A., Gilbert, B.E., Mas, V., Millar, A., Power, U.F., Stortelers, C., Allosery, K., et al. (2016). Generation and characterization of ALX-0171, a potent novel therapeutic nanobody for the treatment of respiratory syncytial virus infection. Antimicrob. Agents Chemother. *60*, 6–13. https://doi.org/10.1128/AAC.01802-15.

Dunbar, J., Krawczyk, K., Leem, J., Baker, T., Fuchs, A., Georges, G., Shi, J., and Deane, C.M. (2014). SAbDab: the structural antibody database. Nucleic Acids Res. *42*, D1140–D1146. https://doi.org/10.1093/nar/gkt1043.

Edgar, R.C. (2004). MUSCLE: a multiple sequence alignment method with reduced time and space complexity. BMC Bioinf. *5*, 113. https://doi.org/10.1186/1471-2105-5-113.

Ekiert, D.C., Friesen, R.H.E., Bhabha, G., Kwaks, T., Jongeneelen, M., Yu, W., Ophorst, C., Cox, F., Korse, H.J., Brandenburg, B., et al. (2011). A highly conserved neutralizing epitope on group 2 influenza A viruses. Science *333*, 843–850. https://doi.org/10.1126/science.1204839.

Emsley, P.C.K. (2004). Coot: model-building tools for molecular graphics. Acta Crystallogr. D Biol. Crystallogr. *60*, 2126–2132. https://doi.org/10.1107/s0907444904019158.

Emsley, P., and Crispin, M. (2018). Structural analysis of glycoproteins: building N-linked glycans with Coot. Acta Crystallogr. D Struct. Biol. *74*, 256–263. https://doi.org/10.1107/S2059798318005119.

Emsley, P., Lohkamp, B., Scott, W.G., and Cowtan, K. (2010). Features and development of Coot. Acta Crystallogr. D Biol. Crystallogr. *66*, 486–501. https://doi.org/10.1107/S0907444910007493.

Feller, S.E., Zhang, Y., Pastor, R.W., and Brooks, B.R. (1995). Constant pressure molecular dynamics simulation: the Langevin piston method. J. Chem. Phys. *103*, 4613–4621. https://doi.org/10.1063/1.470648.

Fridy, P.C., Li, Y., Keegan, S., Thompson, M.K., Nudelman, I., Scheid, J.F., Oeffinger, M., Nussenzweig, M.C., Fenyö, D., Chait, B.T., and Rout, M.P. (2014). A robust pipeline for rapid production of versatile nanobody repertoires. Nat. Methods *11*, 1253–1260. https://doi.org/10.1038/nmeth.3170.

Fu, L., Niu, B., Zhu, Z., Wu, S., and Li, W. (2012). CD-HIT: accelerated for clustering the next-generation sequencing data. Bioinformatics *28*, 3150–3152. https://doi.org/10.1093/bioinformatics/bts565.

Gohlke, H., and Case, D.A. (2004). Converging free energy estimates: MM-PB(GB)SA studies on the protein-protein complex Ras-Raf. J. Comput. Chem. *25*, 238–250. https://doi.org/10.1002/jcc.10379.

Guttler, T., Aksu, M., Dickmanns, A., Stegmann, K.M., Gregor, K., Rees, R., Taxer, W., Rymarenko, O., Schünemann, J., Dienemann, C., et al. (2021). Neutralization of SARS-CoV-2 by highly potent, hyperthermostable, and mutation-tolerant nanobodies. EMBO J. *40*, e107985. https://doi.org/10.15252/embj.2021107985.

Hamers-Casterman, C., Atarhouch, T., Muyldermans, S., Robinson, G., Hamers, C., Songa, E.B., Bendahman, N., and Hammers, R. (1993). Naturally occurring antibodies devoid of light chains. Nature *363*, 446–448. https://doi.org/10.1038/363446a0.

Harvey, W.T., Carabelli, A.M., Jackson, B., Gupta, R.K., Thomson, E.C., Harrison, E.M., Ludden, C., Reeve, R., Rambaut, A., Peacock, S.J., and Robertson, D.L. (2021). SARS-CoV-2 variants, spike mutations and immune escape. Nat. Rev. Microbiol. *19*, 409–424. https://doi.org/10.1038/s41579-021-00573-0.

Hastie, K.M., Li, H., Bedinger, D., Schendel, S.L., Dennison, S.M., Li, K., Rayaprolu, V., Yu, X., Mann, C., Zandonatti, M., et al. (2021). Defining variant-resistant epitopes targeted by SARS-CoV-2 antibodies: a global consortium study. Science *374*, 472–478. https://doi.org/10.1126/science.abh2315.

Hsieh, C.L., Goldsmith, J.A., Schaub, J.M., DiVenere, A.M., Kuo, H.C., Javanmardi, K., Le, K.C., Wrapp, D., Lee, A.G., Liu, Y., et al. (2020). Structure-based design of prefusion-stabilized SARS-CoV-2 spikes. Science *369*, 1501–1505. https://doi.org/10.1126/science.abd0826.

Huang, J., Rauscher, S., Nawrocki, G., Ran, T., Feig, M., de Groot, B.L., Grubmüller, H., and MacKerell, A.D., Jr. (2017). CHARMM36m: an improved force field for folded and intrinsically disordered proteins. Nat. Methods *14*, 71–73. https://doi.org/10.1038/nmeth.4067.

Huo, J., Le Bas, A., Ruza, R.R., Duyvesteyn, H.M.E., Mikolajek, H., Malinauskas, T., Tan, T.K., Rijal, P., Dumoux, M., Ward, P.N., et al. (2020). Neutralizing nanobodies bind SARS-CoV-2 spike RBD and block interaction with ACE2. Nat. Struct. Mol. Biol. *27*, 846–854. https://doi.org/10.1038/s41594-020-0469-6.

Huo, J., Mikolajek, H., Le Bas, A., Clark, J.J., Sharma, P., Kipar, A., Dormon, J., Norman, C., Weckener, M., Clare, D.K., et al. (2021). A potent SARS-CoV-2 neutralising nanobody shows therapeutic efficacy in the Syrian golden hamster model of COVID-19. Nat. Commun. *12*, 5469. https://doi.org/10.1038/s41467-021-25480-z.

Jean-Paul Ryckaert, G.C., Ciccotti, G., and Berendsen, H.J.C. (1977). Numerical integration of the cartesian equations of motion of a system with constraints: molecular dynamics of n-alkanes. J. Comput. Phys. *23*, 327–341. https://doi.org/10.1016/0021-9991(77)90098-5.

Jo, S., Kim, T., Iyer, V.G., and Im, W. (2008). CHARMM-GUI: a web-based graphical user interface for CHARMM. J. Comput. Chem. *29*, 1859–1865. https://doi.org/10.1002/jcc.20945.

Jorgensen, W.L., Chandrasekhar, J., Madura, J.D., Impey, R.W., and Klein, M.L. (1983). Comparison of simple potential functions for simulating liquid water. J. Chem. Phys. *79*, 926–935. https://doi.org/10.1063/1.445869.

Karim, S.S.A., and Karim, Q.A. (2021). Omicron SARS-CoV-2 variant: a new chapter in the COVID-19 pandemic. Lancet *398*, 2126–2128. https://doi.org/10.1016/S0140-6736(21)02758-6.

Kirschner, K.N., Yongye, A.B., Tschampel, S.M., González-Outeiriño, J., Daniels, C.R., Foley, B.L., and Woods, R.J. (2008). GLYCAM06: a generalizable biomolecular force field. Carbohydrates. Carbohydrates. J Comput. Chem. *29*, 622–655. https://doi.org/10.1002/jcc.20820.

Koenig, P.A., Das, H., Liu, H., Kümmerer, B.M., Gohr, F.N., Jenster, L.M., Schiffelers, L.D.J., Tesfamariam, Y.M., Uchima, M., Wuerth, J.D., et al. (2021). Structure-guided multivalent nanobodies block SARS-CoV-2 infection and suppress mutational escape. Science *371*, eabe6230. https://doi.org/10.1126/science.abe6230.

Kollman, P.A., Massova, I., Reyes, C., Kuhn, B., Huo, S., Chong, L., Lee, M., Lee, T., Duan, Y., Wang, W., et al. (2000). Calculating structures and free energies of complex molecules: combining molecular mechanics and continuum models. Acc. Chem. Res. *33*, 889–897. https://doi.org/10.1021/ar000033j.

Kumar, S., Stecher, G., Li, M., Knyaz, C., and Tamura, K. (2018). Mega X: molecular evolutionary genetics analysis across computing Platforms. Mol. Biol. Evol. *35*, 1547–1549. https://doi.org/10.1093/molbev/msy096.

Lan, J., Ge, J., Yu, J., Shan, S., Zhou, H., Fan, S., Zhang, Q., Shi, X., Wang, Q., Zhang, L., and Wang, X. (2020). Structure of the SARS-CoV-2 spike receptor-binding domain bound to the ACE2 receptor. Nature *581*, 215–220. https://doi.org/10.1038/s41586-020-2180-5.

Liu, C., Zhou, Q., Li, Y., Garner, L.V., Watkins, S.P., Carter, L.J., Smoot, J., Gregg, A.C., Daniels, A.D., Jervey, S., and Albaiu, D. (2020a). Research and development on therapeutic agents and vaccines for COVID-19 and related human coronavirus diseases. ACS Cent. Sci. *6*, 315–331. https://doi.org/10.1021/acscentsci.0c00272.

Liu, H., Wu, N.C., Yuan, M., Bangaru, S., Torres, J.L., Caniels, T.G., van Schooten, J., Zhu, X., Lee, C.C.D., Brouwer, P.J.M., et al. (2020b). Cross-neutralization of a SARS-CoV-2 antibody to a functionally conserved site is mediated by avidity. Immunity *53*, 1272–1280.e5. https://doi.org/10.1016/j.immuni.2020.10.023.

Lv, Z., Deng, Y.Q., Ye, Q., Cao, L., Sun, C.Y., Fan, C., Huang, W., Sun, S., Sun, Y., Zhu, L., et al. (2020). Structural basis for neutralization of SARS-CoV-2 and

SARS-CoV by a potent therapeutic antibody. Science 369, 1505–1509. https://doi.org/10.1126/science.abc5881.

Martinez, D.R., Schäfer, A., Gobeil, S., Li, D., De la Cruz, G., Parks, R., Lu, X., Barr, M., Stalls, V., Janowska, K., et al. (2021). A broadly cross-reactive antibody neutralizes and protects against sarbecovirus challenge in mice. Sci. Transl. Med. 14, eabj7125. https://doi.org/10.1126/scitranslmed.abj7125.

Martyna, G.J., Tobias, D.J., and Klein, M.L. (1994). Constant pressure molecular dynamics algorithms. J. Chem. Phys. 101, 4177–4189. https://doi.org/10.1063/1.467468.

Mast, F.D., Fridy, P.C., Ketaren, N.E., Wang, J., Jacobs, E.Y., Olivier, J.P., Sanyal, T., Molloy, K.R., Schmidt, F., Rutkowska, M., et al. (2021). Highly synergistic combinations of nanobodies that target SARS-CoV-2 and are resistant to escape. Elife 10, e73027. https://doi.org/10.7554/eLife.73027.

Mastronarde, D.N. (2005). Automated electron microscope tomography using robust prediction of specimen movements. J. Struct. Biol. 152, 36–51. https://doi.org/10.1016/j.jsb.2005.07.007.

McCoy, A.J., Grosse-Kunstleve, R.W., Adams, P.D., Winn, M.D., Storoni, L.C., and Read, R.J. (2007). Phaser crystallographic software. J. Appl. Crystallogr. 40, 658–674. https://doi.org/10.1107/S0021889807021206.

Meganck, R.M., and Baric, R.S. (2021). Developing therapeutic approaches for twenty-first-century emerging infectious viral diseases. Nat. Med. 27, 401–410. https://doi.org/10.1038/s41591-021-01282-0.

Mehdipour, A.R., and Hummer, G. (2021). Dual nature of human ACE2 glycosylation in binding to SARS-CoV-2 spike. Proc. Natl. Acad. Sci. U.S.A. 118, e2100425118. https://doi.org/10.1073/pnas.2100425118.

Miller, B.R., 3rd, McGee, T.D., Jr., Swails, J.M., Homeyer, N., Gohlke, H., and Roitberg, A.E. (2012). MMPBSA.py: an efficient Program for end-state free energy calculations. J. Chem. Theory Comput. 8, 3314–3321. https://doi.org/10.1021/ct300418h.

Mirdita, M., Schütze, K., Moriwaki, Y., Heo, L., Ovchinnikov, S., and Steinegger, M. (2021). ColabFold - making protein folding accessible to all. Preprint at bioRxiv. https://doi.org/10.1101/2021.08.15.456425.

Mitternacht, S. (2016). FreeSASA: an open source C library for solvent accessible surface area calculations. F1000Res. 5, 189. https://doi.org/10.12688/f1000research.7931.1.

Muyldermans, S. (2013). Nanobodies: natural single-domain antibodies. Annu. Rev. Biochem. 82, 775–797. https://doi.org/10.1146/annurev-biochem-063011-092449.

Nabel, K.G., Clark, S.A., Shankar, S., Pan, J., Clark, L.E., Yang, P., Coscia, A., McKay, L.G.A., Varnum, H.H., Brusic, V., et al. (2021). Structural basis for continued antibody evasion by the SARS-CoV-2 receptor binding domain. Science 375, eabl6251. https://doi.org/10.1126/science.abl6251.

Nakamura, T., Yamada, K.D., Tomii, K., and Katoh, K. (2018). Parallelization of MAFFT for large-scale multiple sequence alignments. Bioinformatics 34, 2490–2492. https://doi.org/10.1093/bioinformatics/bty121.

Nambulli, S., Xiang, Y., Tilston-Lunel, N.L., Rennick, L.J., Sang, Z., Klimstra, W.B., Reed, D.S., Crossland, N.A., Shi, Y., and Duprex, W.P. (2021). Inhalable Nanobody (PiN-21) prevents and treats SARS-CoV-2 infections in Syrian hamsters at ultra-low doses. Sci. Adv. 7, eabh0319. https://doi.org/10.1126/sciadv.abh0319.

Otwinowski, Z., and Minor, W. (1997). Processing of X-ray diffraction data collected in oscillation mode. Methods Enzymol. 276, 307–326. https://doi.org/10.1016/S0076-6879(97)76066-X.

Pettersen, E.F., Goddard, T.D., Huang, C.C., Meng, E.C., Couch, G.S., Croll, T.I., Morris, J.H., and Ferrin, T.E. (2021). UCSF ChimeraX: structure visualization for researchers, educators, and researchers. Protein Sci. 30, 70–82. https://doi.org/10.1002/pro.3943.

Phillips, J.C., Braun, R., Wang, W., Gumbart, J., Tajkhorshid, E., Villa, E., Chipot, C., Skeel, R.D., Kalé, L., and Schulten, K. (2005). Scalable molecular dynamics with NAMD. J. Comput. Chem. 26, 1781–1802. https://doi.org/10.1002/jcc.20289.

Piccoli, L., Park, Y.J., Tortorici, M.A., Czudnochowski, N., Walls, A.C., Beltramello, M., Silacci-Fregni, C., Pinto, D., Rosen, L.E., Bowen, J.E., et al. (2020).

Mapping neutralizing and immunodominant sites on the SARS-CoV-2 spike receptor-binding domain by structure-guided high-resolution serology. Cell 183, 1024–1042.e21. https://doi.org/10.1016/j.cell.2020.09.037.

Pinto, D., Park, Y.J., Beltramello, M., Walls, A.C., Tortorici, M.A., Bianchi, S., Jaconi, S., Culap, K., Zatta, F., De Marco, A., et al. (2020). Cross-neutralization of SARS-CoV-2 by a human monoclonal SARS-CoV antibody. Nature 583, 290–295. https://doi.org/10.1038/s41586-020-2349-y.

Punjani, A., and Fleet, D.J. (2021). 3D variability analysis: resolving continuous flexibility and discrete heterogeneity from single particle cryo-EM. J. Struct. Biol. 213, 107702. https://doi.org/10.1016/j.jsb.2021.107702.

Punjani, A., Rubinstein, J.L., Fleet, D.J., and Brubaker, M.A. (2017). cryoSPARC: algorithms for rapid unsupervised cryo-EM structure determination. Nat. Methods 14, 290–296. https://doi.org/10.1038/nmeth.4169.

Punjani, A., Zhang, H., and Fleet, D.J. (2020). Non-uniform refinement: adaptive regularization improves single-particle cryo-EM reconstruction. Nat. Methods 17, 1214–1221. https://doi.org/10.1038/s41592-020-00990-8.

Pymm, P., Adair, A., Chan, L.J., Cooney, J.P., Mordant, F.L., Allison, C.C., Lopez, E., Haycroft, E.R., O'Neill, M.T., Tan, L.L., et al. (2021). Nanobody cocktails potently neutralize SARS-CoV-2 D614G N501Y variant and protect mice. Proc. Natl. Acad. Sci. U.S.A. 118, e2101918118. https://doi.org/10.1073/pnas.2101918118.

Rappazzo, C.G., Tse, L.V., Kaku, C.I., Wrapp, D., Sakharkar, M., Huang, D., Deveau, L.M., Yockachonis, T.J., Herbert, A.S., Battles, M.B., et al. (2021). Broad and potent activity against SARS-like viruses by an engineered human monoclonal antibody. Science 371, 823–829. https://doi.org/10.1126/science.abf4830.

Regev-Yochay, G., Gonen, T., Gilboa, M., Mandelboim, M., Indenbaum, V., Amit, S., Meltzer, L., Asraf, K., Cohen, C., Fluss, R., et al. (2022). Efficacy of a fourth dose of Covid-19 mRNA vaccine against Omicron. N. Engl. J. Med. 386, 1377–1380. https://doi.org/10.1056/NEJMc2202542.

Scheres, S.H.W., and Chen, S. (2012). Prevention of overfitting in cryo-EM structure determination. Nat. Methods 9, 853–854. https://doi.org/10.1038/nmeth.2115.

Schmidt, F., Weisblum, Y., Rutkowska, M., Poston, D., DaSilva, J., Zhang, F., Bednarski, E., Cho, A., Schaefer-Babajew, D.J., Gaebler, C., et al. (2021). High genetic barrier to SARS-CoV-2 polyclonal neutralizing antibody escape. Nature 600, 512–516. https://doi.org/10.1038/s41586-021-04005-0.

Schoof, M., Faust, B., Saunders, R.A., Sangwan, S., Rezelj, V., Hoppe, N., Boone, M., Billesbølle, C.B., Puchades, C., Azumaya, C.M., et al. (2020). An ultrapotent synthetic nanobody neutralizes SARS-CoV-2 by stabilizing inactive Spike. Science 370, 1473–1479. https://doi.org/10.1126/science.abe3255.

Sok, D., and Burton, D.R. (2018). Recent progress in broadly neutralizing antibodies to HIV. Nat. Immunol. 19, 1179–1188. https://doi.org/10.1038/s41590-018-0235-7.

Stamatatos, L., Czartoski, J., Wan, Y.H., Homad, L.J., Rubin, V., Glantz, H., Neradilek, M., Seydoux, E., Jennewein, M.F., MacCamy, A.J., et al. (2021). mRNA vaccination boosts cross-variant neutralizing antibodies elicited by SARS-CoV-2 infection. Science 372, 1413–1418. https://doi.org/10.1126/science.abg9175.

Starr, T.N., Czudnochowski, N., Liu, Z., Zatta, F., Park, Y.J., Addetia, A., Pinto, D., Beltramello, M., Hernandez, P., Greaney, A.J., et al. (2021). SARS-CoV-2 RBD antibodies that maximize breadth and resistance to escape. Nature 597, 97–102. https://doi.org/10.1038/s41586-021-03807-6.

Starr, T.N., Greaney, A.J., Hilton, S.K., Ellis, D., Crawford, K.H.D., Dingens, A.S., Navarro, M.J., Bowen, J.E., Tortorici, M.A., Walls, A.C., et al. (2020). Deep mutational scanning of SARS-CoV-2 receptor binding domain reveals constraints on folding and ACE2 binding. Cell 182, 1295–1310.e20. https://doi.org/10.1016/j.cell.2020.08.012.

Steinegger, M., Meier, M., Mirdita, M., Vöhringer, H., Haunsberger, S.J., and Söding, J. (2019). HH-suite3 for fast remote homology detection and deep protein annotation. BMC Bioinf. 20, 473. https://doi.org/10.1186/s12859-019-3019-7.

Sun, D., Sang, Z., Kim, Y.J., Xiang, Y., Cohen, T., Belford, A.K., Huet, A., Conway, J.F., Sun, J., Taylor, D.J., et al. (2021). Potent neutralizing nanobodies resist convergent circulating variants of SARS-CoV-2 by targeting diverse and conserved epitopes. Nat. Commun. *12*, 4676. https://doi.org/10.1038/s41467-021-24963-3.

Tian, C., Kasavajhala, K., Belfon, K.A.A., Raguette, L., Huang, H., Migues, A.N., Bickel, J., Wang, Y., Pincay, J., Wu, Q., and Simmerling, C. (2020). ff19SB: amino-acid-specific protein backbone parameters trained against quantum mechanics energy surfaces in solution. J. Chem. Theory Comput. *16*, 528–552. https://doi.org/10.1021/acs.jctc.9b00591.

Tortorici, M.A., Czudnochowski, N., Starr, T.N., Marzi, R., Walls, A.C., Zatta, F., Bowen, J.E., Jaconi, S., Di Iulio, J., Wang, Z., et al. (2021). Broad sarbecovirus neutralization by a human monoclonal antibody. Nature *597*, 103–108. https://doi.org/10.1038/s41586-021-03817-4.

Tubiana, J., Schneidman-Duhovny, D., and Wolfson, H.J. (2021). ScanNet: an interpretable geometric deep learning model for structure-based protein binding site prediction. Preprint at bioRxiv. https://doi.org/10.1101/2021.09.05.459013.

Vanlandschoot, P., Stortelers, C., Beirnaert, E., Ibañez, L.I., Schepens, B., Depla, E., and Saelens, X. (2011). Nanobodies®: new ammunition to battle viruses. Antiviral Res. *92*, 389–407. https://doi.org/10.1016/j.antiviral.2011.09.002.

Wagner, T.R., Ostertag, E., Kaiser, P.D., Gramlich, M., Ruetalo, N., Junker, D., Haering, J., Traenkle, B., Becker, M., Dulovic, A., et al. (2021). Neutrobody-Plex-monitoring SARS-CoV-2 neutralizing immune responses using nanobodies. EMBO Rep. *22*, e52325. https://doi.org/10.15252/embr.202052325.

Walker, L.M., and Burton, D.R. (2018). Passive immunotherapy of viral infections: 'super-antibodies' enter the fray. Nat. Rev. Immunol. *18*, 297–308. https://doi.org/10.1038/nri.2017.148.

Walls, A.C., Park, Y.J., Tortorici, M.A., Wall, A., McGuire, A.T., and Veesler, D. (2020). Structure, function, and antigenicity of the SARS-CoV-2 spike glycoprotein. Cell *181*, 281–292.e6. https://doi.org/10.1016/j.cell.2020.02.058.

Wang, Z., Muecksch, F., Schaefer-Babajew, D., Finkin, S., Viant, C., Gaebler, C., Hoffmann, H.H., Barnes, C.O., Cipolla, M., Ramos, V., et al. (2021). Naturally enhanced neutralizing breadth against SARS-CoV-2 one year after infection. Nature *595*, 426–431. https://doi.org/10.1038/s41586-021-03696-9.

Watanabe, Y., Berndsen, Z.T., Raghwani, J., Seabright, G.E., Allen, J.D., Pybus, O.G., McLellan, J.S., Wilson, I.A., Bowden, T.A., Ward, A.B., and Crispin, M. (2020). Vulnerabilities in coronavirus glycan shields despite extensive glycosylation. Nat. Commun. *11*, 2688. https://doi.org/10.1038/s41467-020-16567-0.

Williams, C.J., Headd, J.J., Moriarty, N.W., Prisant, M.G., Videau, L.L., Deis, L.N., Verma, V., Keedy, D.A., Hintze, B.J., Chen, V.B., et al. (2018). MolProbity: more and better reference data for improved all-atom structure validation. Protein Sci. *27*, 293–315. https://doi.org/10.1002/pro.3330.

Wolfel, R., Corman, V.M., Guggemos, W., Seilmaier, M., Zange, S., Müller, M.A., Niemeyer, D., Jones, T.C., Vollmar, P., Rothe, C., et al. (2020). Virological assessment of hospitalized patients with COVID-2019. Nature *581*, 465–469. https://doi.org/10.1038/s41586-020-2196-x.

Xiang, Y., Nambulli, S., Xiao, Z., Liu, H., Sang, Z., Duprex, W.P., Schneidman-Duhovny, D., Zhang, C., and Shi, Y. (2020). Versatile and multivalent nanobodies efficiently neutralize SARS-CoV-2. Science *370*, 1479–1484. https://doi.org/10.1126/science.abe4747.

Xiang, Y., Sang, Z., Bitton, L., Xu, J., Liu, Y., Schneidman-Duhovny, D., and Shi, Y. (2021). Integrative proteomics identifies thousands of distinct, multi-epitope, and high-affinity nanobodies. Cell Syst. *12*, 220–234.e9. https://doi.org/10.1016/j.cels.2021.01.003.

Xu, J., Xu, K., Jung, S., Conte, A., Lieberman, J., Muecksch, F., Lorenzi, J.C.C., Park, S., Schmidt, F., Wang, Z., et al. (2021). Nanobodies from camelid mice and llamas neutralize SARS-CoV-2 variants. Nature *595*, 278–282. https://doi.org/10.1038/s41586-021-03676-z.

Ye, G., Gallant, J., Zheng, J., Massey, C., Shi, K., Tai, W., Odle, A., Vickers, M., Shang, J., Wan, Y., et al. (2021). The development of Nanosota-1 as anti-SARS-CoV-2 nanobody drug candidates. Elife *10*, e64815. https://doi.org/10.7554/eLife.64815.

Yuan, M., Wu, N.C., Zhu, X., Lee, C.C.D., So, R.T.Y., Lv, H., Mok, C.K.P., and Wilson, I.A. (2020). A highly conserved cryptic epitope in the receptor binding domains of SARS-CoV-2 and SARS-CoV. Science *368*, 630–633. https://doi.org/10.1126/science.abb7269.

Zivanov, J., Nakane, T., Forsberg, B.O., Kimanius, D., Hagen, W.J., Lindahl, E., and Scheres, S.H. (2018). New tools for automated high-resolution cryo-EM structure determination in RELION-3. Elife *7*, e42166. https://doi.org/10.7554/eLife.42166.

STAR★METHODS

KEY RESOURCES TABLE

REAGENT or RESOURCE	SOURCE	IDENTIFIER
Antibodies		
Llama IgG-H+L Antibody [HRP], pAb, Goat	Bethyl	Cat# A160-100P; RRID: AB_67107
T7 Tag Polyclonal Antibody, HRP	Thermo Fisher	Cat# PA1-31449; RRID: AB_1960906
Pierce™ High Sensitivity NeutrAvidin™-HRP	Thermo Fisher	Cat# 31030; RRID: N/A
Bacterial and virus strains		
One Shot™ BL21(DE3) Chemically Competent *E. coli*	Invitrogen	C600003
SARS-CoV-2 Delta strain	BEI	NR55611
SARS-CoV-2 Munich strain	(Wolfel et al., 2020)	N/A
Biological samples		
Llama Wally bleed, 10 days after the 3rd and 8th boost	Caprologics, Inc.	N/A
SARS-CoV, SARS-CoV-2 and variants pseudovirus particles (luciferase reporter)	Integral Molecular	RVP-702L, 706L, 707L, 763L, 766L, 768L, 801L
Chemicals, peptides, and recombinant proteins		
SARS-CoV-2 RBD-Fc	Acro Biosystems	SPD-c5255
Pierce™ Lys-C Protease, MS Grade	Thermo Fisher	90051
Chymotrypsin, Sequencing Grade	Promega	V1061
Sequencing Grade Modified Trypsin	Promega	V5111
Formic Acid, 99+%	Thermo Fisher	PI28905
Water, Optima™ LC/MS Grade	Fisher Scientific	W6-1
Water with 0.1% Formic Acid (v/v), Optima™ LC/MS Grade	Fisher Scientific	LS118-1
Pierce™ Acetonitrile (ACN), LC/MS Grade	Thermo Fisher	85188
Pierce™ 0.1% Formic Acid (v/v) in Acetonitrile (ACN), LC/MS Grade	Thermo Fisher	85175
LB Miller Broth	IBI Scientific	49030
Ampicillin, sodium salt, irradiated	Gibco	11593027
LB Miller's Agar Powder	Growcells.com	MBPE-3020
Dulbecco's phosphate buffer saline no Ca 2+, Mg 2+	Thermo Fisher	14190250
Pierce™ Protease Inhibitor Tablets, EDTA-free	Thermo Fisher	A32965
Tween® 20	Sigma	P9416-100mL
Histopaque® - 1077, sterile-filtered, 1.077g/mL	Sigma	10771-500 mL
Puromycin	Gibco	A1113803
Penicillin-Streptomycin Solution, 100 x	Corning	30-002-Cl
Critical commercial assays		
RNeasy® Mini & Maxi Kit	Qiagen	74106; 75142
Monarch® PCR & DNA Cleanup Kit	NEB	T1030L
Monarch® DNA Gel Extraction Kit	NEB	T1020S
Maxima™ H Minus cDNA Synthesis kit	Thermo Fisher	K1682
Platinum™ SuperFi™ PCR Master Mix	Thermo Fisher	12358050
ELISA kit	R & D system	DY990-999
Biacore 3000 kits	GE Healthcare	Multiple
ExpiFectamine 293 kit	Thermo Fisher	A14635
Renilla-Glo luciferase assay system	Promega	E2720

(Continued on next page)

Continued

REAGENT or RESOURCE	SOURCE	IDENTIFIER
Deposited data		
Codes for analysis (related to Figures 1, 3 and 6)	This paper; Github	https://github.com/yishi-lab/Super-immunity-by-pan-sarbecovirus-nanobodies
Experimental models: Cell lines		
Expi293F cells	Thermo Fisher	A14635
Vero-E6 cell	ATCC	Cat# CRL-1586™; RRID: CVCL_0574
Vero-E6-TMPRSS2-T2A-ACE2 cell	ATCC	NR-54907
293T-hsACE2	Integral Molecular	C-HA101
Oligonucleotides		
Dprimer1: 5′-cccAAGCTTggtggtggtggtagtggtggtggtggtagtggtggtggtggtagtCAaGTTCAACTGGTTGAATCTG-3′	This paper	N/A
Dprimer2: 5′ccgCTCGAGTGCGGCCGCcagtttGCTACTAACGGTAACTT-3′	This paper	N/A
Recombinant DNA		
p3BNC vectors bearing sarbecovirus RBDs	(Cohen et al., 2021)	N/A
SARS-CoV-2 Hexapro spike	Addgene	154754
p3BNC vectors bearing rest RBDs	Synbio	N/A
Multiple Nanobodies in pET-21b(+) vector	Synbio	N/A
Software and algorithms		
Proteome Discoverer 1.2	Thermo Fisher	N/A
Prism Version 9	GraphPad Software	https://www.graphpad.com/scientific-software/prism/
BioPython	N/A	https://biopython.org/
AugurLlama	(Xiang et al., 2020)	https://github.com/yishi-lab/AugurLlama
ScanNet	(Tubiana et al., 2021)	http://bioinfo3d.cs.tau.ac.il/ScanNet/
CD-HIT	(Fu et al., 2012)	http://weizhong-lab.ucsd.edu/cd-hit/
COOT	(Emsley and Crispin, 2018; Emsley et al., 2010; Emsley, 2004)	https://www2.mrc-lmb.cam.ac.uk/personal/pemsley/coot/
serialEM	(Mastronarde, 2005)	https://bio3d.colorado.edu/SerialEM/
CryoSPARC	(Punjani and Fleet, 2021; Punjani et al., 2017; Punjani et al., 2020)	https://cryosparc.com
ColabFold	(Mirdita et al., 2021)	https://github.com/sokrypton/ColabFold
Phenix	(Afonine et al., 2018)	https://phenix-online.org
ChimeraX	(Pettersen et al., 2021)	https://www.cgl.ucsf.edu/chimerax/
RELION 3.1	(Zivanov et al., 2018)	https://www3.mrc-lmb.cam.ac.uk/relion/index.php/Main_Page
Tleap	(Case et al., 2005)	http://ambermd.org/tutorials/pengfei/
NAMD	(Phillips et al., 2005)	https://www.ks.uiuc.edu/Research/namd/v
PHASER	(McCoy et al., 2007)	https://www.phaser.cimr.cam.ac.uk/index.php/Phaser_Crystallographic_Software
MAFFT	(Nakamura et al., 2018)	https://mafft.cbrc.jp/alignment/software/
HHBlits	(Steinegger et al., 2019)	https://toolkit.tuebingen.mpg.de/tools/hhblits
HKL2000	(Otwinowski and Minor, 1997)	N/A
MolProbity	(Williams et al., 2018)	N/A
Gromacs Version 2020	(Huang et al., 2017)	https://www.gromacs.org
MUSCLE	(Edgar, 2004)	https://www.drive5.com/muscle/
MEGA	(Kumar et al., 2018)	https://www.megasoftware.net

(*Continued on next page*)

Continued

REAGENT or RESOURCE	SOURCE	IDENTIFIER
FreeSASA	(Mitternacht, 2016)	https://freesasa.github.io
CHARMM-GUI webserver	(Jo et al., 2008)	https://www.charmm-gui.org
Others		
Sep-Pak C18 1cc Vac Cartridge, 55 – 105 μm, 50 mg	Waters	WAT054955
Empore™ SPE Disks C18, Diam. 47 mm	Sigma	66883-U
PROTEINDEX™ rProtein G Agarose 4 Fast Flow	Marvelgent Biosciences, Inc.	11-0206-025
PROTEINDEX™ rProtein A Agarose 4 Fast Flow	Marvelgent Biosciences, Inc.	11-0203-025
CNBr - Activated Sepharose™ 4 Fast Flow Affinity Media	GE Healthcare	17098101
HisPur™ Cobalt Resin	Thermo Fisher	89966

RESOURCE AVAILABILITY

Lead contact

Further information and requests for resources and agents should be directed to and will be fulfilled by the lead contact, Y.S. (wally.yis@gmail.com).

Materials availability

Plasmids of psNbs can be requested from lead contact. The protein sequences of the psNbs are also available in Table S6.

Data and code availability

Atomic coordinates X-ray/electron cryo-microscopy structures in this paper have been deposited to the Protein Data Bank (PDB). PDB: 8CYA (2-67:spike), 8CYC (2-34:spike), 8CY7 (2-38:spike), 8CXN (2-57:spike), 8CYB (1-8:spike), 8CXQ (1-22:spike), 8CY9 (1-23:spike), 8CY6 (2-65:spike), 8CYD (2-45:spike), 8CYJ (2-10:2-67:2-62:spike), 8CWU (1-21:RBD), and 8CWV (2-31:RBD:CC12.1Fab). The accession numbers and more detailed informations are also available in Tables S2 and S3.

The codes for the analysis are available from Github at https://github.com/yishi-lab/Super-immunity-by-pan-sarbecovirus-nanobodies.

Any additional information required to reanalyze the data reported in this paper is available from the lead contact upon request.

EXPERIMENTAL MODEL AND SUBJECT DETAILS

The 293T-hsACE2 stable cell line was purchased from Integral Molecular in the freezing media (50% cell culture media, 40% FBS, 10% DMSO). Cells were cultured in a cell culture media (DMEM, 10%FBS, 10 mM HEPES, 1x Penicillin-Streptomycin and 0.5 μg/mL Puromycin) at 37°C, 5% (v/v) CO_2. Cells were split once 80–90% confluency has been reached. After at least three passages, cells were used for the pseudovirus neutralization assay at 80–90% confluency and more than 95% viability. The cell line was authenticated by the Integral Molecular using the flow cytometry by an ACE2 specific monoclonal antibody (R&D system, cat# MAB9332-100).

The Expi293F cells were obtained from Thermo Fisher. 1 mL of the cells were thawed at 37°C water bath and added to 29 mL of pre-warmed Expi293 Expression Media in a 125 mL non-baffled, vented flask. The cells were cultured at 37°C, 8% (v/v) CO_2 on an orbital shaker at 120 r.p.m. Cells were split when density reached to 3–5 × 10e6 cells/mL. At least three passages were performed, and more than 98% cell viability were ensured before the transfection. The authentication of the cell line was not performed in our hands.

Vero E6 cell or Vero E6-TMPRSS2-T2A-ACE2 cells were purchased from ATCC and were grown in DMEM (Dulbecco's Modified Eagle Medium; Corning) supplemented with 10 % (v/v) fetal bovine serum (FBS; Atlanta Biologicals), 1 % (v/v) l-glutamine (Corning) and 1 % (v/v) penicillin/streptomycin (pen-strep; Corning).

The virus was diluted to 500 μL in 15 mL with virus dilution medium (Opti-MEM, Gibco) supplemented with 2% (v/v) FBS and added to a confluent monolayer of Vero E6 cells in an expanded-surface 1900 cm² roller bottle (CELLTREAT Scientific Products), resulting in a multiplicity of infection (m.o.i.) of 0.0004. After 1 hour of incubation at 37°C, 5% (v/v) CO2, 45 mL of virus growth medium (DMEM supplemented with 10% (v/v) FBS, 1% (v/v) l-glutamine and 1% (v/v) pen-strep) was added and cells were incubated under the same conditions for 96 hours. Virus-containing supernatant was collected and clarified by centrifugation at 3500 r.p.m. for 30 minutes at 4°C. The cleared virus supernatant was aliquoted and stored at −80°C for later use.

METHOD DETAILS

Purification of recombinant sarbecovirus RBDs and SARS-CoV-2 spike

The mammalian expression vectors encoding the RBDs of RaTG13-CoV (GenBank QHR63300; S protein residues 319–541), SHC014-CoV (GenBank KC881005; residues 307–524), Rs4081-CoV (GenBank KY417143; residues 310–515), pangolin17-CoV (GenBank QIA48632; residues 317–539), RmYN02-CoV (GSAID EPI_ISL_412977; residues 298–503), Rf1-CoV (GenBank DQ412042; residues 310–515), W1V1-CoV (GenBank KF367457; residues 307–528), Yun11-CoV (GenBank JX993988; residues 310–515), BM-4831-CoV (GenBank NC014470; residues 310–530), BtKY72-CoV (GenBank KY352407; residues 309–530) with an N-terminal Mu phosphatase signal peptide and C-terminal His-tag were a kind gift from Pamela J. Bjorkman's lab, Caltech. Plasmids of the RBDs for the following sarbecovirus strains were synthesized from Synbio Technologies in a similar way: SARS-CoV-2 (GenBank MN985325.1; S protein residues 319–539), SARS-CoV (GenBank AAP13441.1; residues 318–510), Rs7327-CoV (GenBank KY417151.1; residues 319–518), Rs4092-CoV (GenBank KY417145.1; residues 314–496), YN2013-CoV (GenBank KJ473816.1; residues 314–496), ZC45-CoV (GenBank MG772933.1; residues 327–509), HKU3-1-CoV (GenBank DQ022305.2; residues 322–505), Shaanxi2011-CoV (GenBank JX993987.1; residues 321–502) and Rp3-CoV (GenBank DQ071615.1; residues 322–504). The cDNA encoding SARS-CoV-2 spike HexaPro (S) was obtained from Addgene (Hsieh et al., 2020). To express the proteins, Expi293F cells were transiently transfected with the plasmid using the ExpiFectamine 293 kit. After 24 hrs of transfection, enhancers were added to further boost protein expression. Cell culture was harvested 5–6 days after transfection and the supernatant was collected by high-speed centrifugation at 21,000×g for 30 min. The secreted proteins in the supernatant were purified using His-Cobalt resin. Eluted proteins were then concentrated and further purified by size-exclusion chromatography using a Superose 6 10/300 (for S) or Superdex 75 column (for RBDs, Cytiva) in a buffer composed of 20 mM Hepes pH 7.5 and 150 mM NaCl. SARS-CoV-2 RBD variants were obtained from the Acro Biosystems.

Successive camelid immunization with RBD and the proteomic identification of psNbs

A llama ("Wally") was immunized with a SARS-CoV-2 RBD-Fc fusion protein at a primary dose of 0.2 mg (with complete Freund's adjuvant), followed by three consecutive boosts of 0.1 mg every 2 weeks. The initial bleed was collected 10 days after the final boost as previously described (Xiang et al., 2020). Three weeks after the collection of the initial bleed, the llama was immunized again by four consecutive boosts every 2 weeks. The booster bleed was collected 10 days after the final boost. The immunization procedures were performed by Capralogics, Inc. following the IACUC protocol.

To isolate V_HH antibodies, plasma was first purified from the immunized bleeds by the Ficoll gradient (Sigma). Polyclonal V_HHs mixtures were then isolated from the plasma using a two-step purification protocol (Fridy et al., 2014). RBDs from 4 sarbecovirus clades (RBDSARS-CoV-2, RBDSARS-CoV, RBDRmYN02 and RBDBM-4831) were coupled to the CNBr-activated sepharose resin for affinity isolation of RBD-specific V_HHs. After binding, RBD-specific V_HHs were eluted and proteolyzed as previously described (Xiang et al., 2020, 2021). Efficiently digested peptides were subjected to proteomics analysis by using the nano-LC 1200 that was coupled online with a Q Exactive™ HF-X Hybrid Quadrupole Orbitrap™ mass spectrometer. The MS data obtained from different RBD-specific V_HH isolations were analyzed by *AugurLlama* to identify high-affinity Nbs for each RBD (Xiang et al., 2021). To facilitate the identification of psNbs, the abundance of Nb CDR3 peptides was quantified across different V_HH isolations. psNbs (represented by CDR3s) are assigned based on two criteria. 1) they must be classified as high-affinity binders for RBD$_{SARS-CoV-2}$. 2) In addition, they must appear in at least one more RBD isolation sample and are not classified as low affinity binders (Xiang et al., 2021).

Nb DNA synthesis and cloning

The monomeric Nb genes were codon-optimized and synthesized. All the Nb DNA sequences were cloned into a pET-21b(+) vector using EcoRI and HindIII restriction sites. The monomeric Nbs 2–31 and 2–45 were also cloned into a pET-22b(+) vector at the BamHI and XhoI sites for periplasmic expression. To produce a heterodimeric PiN-31, the DNA fragment of the monomeric Nb 2–31 was first PCR amplified from the pET-21b(+) vector by using Dprimer 1 and 2 to introduce a linker sequence and two restriction sites of XhoI and HindIII that facilitate cloning. The PCR fragment was then inserted into the 2–45 pET-21b(+) vector at the same restriction sites to produce the heterodimer PiN-31 (i.e., 2-45-(GGGGS)$_3$-2-31).

Purification of Nbs

Nb DNA constructs were transformed into BL21(DE3) cells and plated on Agar with 50 μg/mL ampicillin at 37°C overnight. Cells were cultured in an LB broth to reach an O.D. of ∼0.5–0.6 before IPTG (0.5–1 mM) induction at 16/20°C overnight. Cells were then harvested, sonicated, and lysed on ice with a lysis buffer (1xPBS, 150 mM NaCl, 0.2% TX-100 with protease inhibitor). After cell lysis, protein extracts were collected by centrifugation at 21,000 x g for 10 mins and the his-tagged Nbs were purified by the Cobalt resin (Thermo) and natively eluted with a buffer containing 150 mM imidazole buffer. Eluted Nbs were subsequently dialyzed in a dialysis buffer (e.g., 1x DPBS, pH 7.4 or SEC buffer).

For the periplasmic preparation of Nbs (2–31 and 2–45), cell pellets were resuspended in the TES buffer (0.1 M Tris-HCl, pH 8.0; 0.25 mM EDTA, pH 8.0; 0.25 M Sucrose) and incubated on ice for 30 min. The supernatants were collected by centrifugation and subsequently dialyzed to DPBS. The resulting Nbs were then purified by Cobalt resin as described above.

ELISA (enzyme-linked immunosorbent assay)

Indirect ELISA was carried out to evaluate the camelid immune responses of the total single-chain only antibody (V_HH) to an RBD and to quantify the relative affinities of the psNbs. A 96-well ELISA plate (R&D system) was coated with the RBD protein or the HEK-293T cell lysate at an amount of approximately 3–5 ng per well in a coating buffer (15 mM sodium carbonate, 35 mM sodium bicarbonate, pH 9.6) overnight at $4°C$, with subsequent blockage with a blocking buffer (DPBS, v/v 0.05% Tween 20, 5% milk) at room temperature for 2 hours. To test the immune response, the total V_HH was serially 5-fold diluted in the blocking buffer and then incubated with the RBD-coated wells at room temperature for 2 hours. HRP-conjugated secondary antibodies against llama Fc were diluted 1:75,00 in the blocking buffer and incubated with each well for an additional 1 hour at room temperature. For the initial screening of Nb binding against 4 RBDs, scramble Nbs that do not bind the RBDs were used as negative controls. Nbs were serially 10-fold diluted from 1 μM to 1 nM in the blocking buffer. For the Nb affinity measurements against 24 RBDs, Nbs were serially 4-fold diluted. The dilutions were incubated for 2 hours at room temperature. HRP-conjugated secondary antibodies against the T7-tag were diluted at 1:5,000 in the blocking buffer and incubated for 1 hour at room temperature. Three washes with 1x PBST (DPBS, v/v 0.05% Tween 20) were carried out to remove nonspecific absorbances between each incubation. After the final wash, the samples were further incubated in the dark with freshly prepared w3,3′,5,5′-Tetramethylbenzidine (TMB) substrate for 10 mins at room temperature to develop the signals. After the STOP solution (R&D system), the plates were read at multiple wavelengths (450 nm and 550 nm) on a plate reader (Multiskan GO, Thermo Fisher). The raw data were processed by Prism 9 (GraphPad) to fit into a 4PL curve and to calculate $logIC_{50}$.

Competitive ELISA with recombinant hACE2

A 96-well plate was pre-coated with recombinant spike-6P at 2 μg/mL at $4°C$ overnight. Nbs were 5-fold diluted (from 0.2/1/5 μM to 12.8/64/320pM) in the assay buffer with a final amount of 50 ng biotinylated hACE2 at each concentration and then incubated with the plate at room temperature for 2 hrs. The plate was washed by the washing buffer to remove the unbound hACE2. 1:6000 diluted Pierce™ High Sensitivity NeutrAvidin™-HRP were incubated with the plate for 1 hr at room temperature. TMB solution was added to react with the HRP conjugates for 10 mins. The reaction was then stopped by the Stop Solution. The signal corresponding to the amount of the bound hACE2 was measured by a plate reader at 450 nm and 550 nm. The wells without Nbs were used as control to calculate the percentage of hACE2 signal. The resulting data were analyzed by Prism 9 (GraphPad) and plotted.

psNb epitope analysis by competitive size exclusion chromatography (SEC)

Analytical size exclusion chromatography was performed with a Superdex 75 increase GL column (column volume: 24 mL, Cytiva) on a Shimadzu HPLC system equipped with a multi-wavelength UV detector at a flow rate of 0.3 mL/min. The column was connected and placed in a column oven set to $15°C$, and the SEC running buffer was 10 mM HEPES pH 7.1, 150 mM NaCl. A reference SEC profile for RBD with epitope I benchmark Nb (Nb21), epitope II benchmark Nb (Nb105) and epitope III benchmark Nb (Nb36) was performed after column equilibration. Subsequently, three separate runs with RBD and specified psNb were performed after mixing with (i) benmark I and benchmark II, (ii) benchmark II and III and (iii) benchmark I and III Nbs. A supershift of the peak, at the same or to the left of the RBD and three Nbs peak in the reference profile, in run (i) but not run (ii) and (iii) sorts a psNb into group C. Similarly, psNb with a supershift in run (ii) but not run (i) and (iii) belongs to group A, and a supershift in run (iii) but not run (i) and (ii) belongs to group B. When supershifts were observed in all three runs, the psNb was sorted into a group D. psNbs were sorted into group E if the supershifts were not detected on SEC.

Nb affinity measurement by SPR

Surface plasmon resonance (SPR, Biacore 3000 system, GE Healthcare) was used to measure Nb affinities. RBD proteins were immobilized on the activated CM5 sensor-chip in pH 4.0 10 mM sodium acetate buffer. The surface of the sensor chip was blocked by 1 M Tris-HCl (pH 8.5). For each Nb analyte, a series of concentration dilutions was injected in HBS-EP running buffer (GE-Healthcare), at a flow rate of 20 μL/min for 180 s, followed by a dissociation time of 15 mins. Between each injection, the sensor chip surface was regenerated with the low pH buffer containing 10 mM glycine-HCl (pH 1.5–2.0). The regeneration was performed with a flow rate of 30–40 μL/min for 30–45 s. The measurements were duplicated, and only highly reproducible data were used for analysis. Binding sensorgrams for each Nb were processed and analyzed using BIAevaluation by fitting with the 1:1 Langmuir model or the 1:1 Langmuir model with the drifting baseline.

Pseudotyped SARS-CoV-2 neutralization assay

The 293T-hsACE2 stable cell line and pseudotyped SARS-CoV-2 (Wuhan-Hu-1 strain, D614G, Alpha, Beta, Lambda, Delta and Omicron) particles with luciferase reporters were purchased from the Integral Molecular. The neutralization assay was carried out according to the manufacturers' protocols. In brief, 3- or 5-fold serially diluted Nbs/immunized V_HH mixture was incubated with the pseudotyped SARS-CoV-2-luciferase for accurate measurements. At least seven concentrations were tested for each Nb and at least two repeats of each Nb were done. Pseudovirus in culture media without Nbs was used as a negative control. 100 μL of the mixtures were then incubated with 100 μL 293T-hsACE2 cells at $2.5 \times 10e^5$ cells/mL in the 96-well plates. The infection took ~72 hrs at $37°C$ with 5% CO_2. The luciferase signal was measured using the *Renilla*-Glo luciferase assay system with the luminometer at 1 ms integration time. The obtained relative luminescence signals (RLU) from the negative control wells were normalized and

used to calculate the neutralization percentage at each concentration. Data were processed by Prism 9 (GraphPad) to fit into a 4PL curve and to calculate the $logIC_{50}$ (half-maximal inhibitory concentration).

SARS-CoV-2 Munich and Delta plaque reduction neutralization test (PRNT)

Nbs were diluted in a 3- or 5-fold series in Opti-MEM (Thermo). Each Nb dilution (110 µL) was mixed with 110 µL of SARS-CoV-2 containing 100 plaque-forming units (p.f.u.) or 110 µL of SARS-CoV-2 containing 50 p.f.u. of the virus in Opti-MEM. The Nb–virus mixes (220 µL total) were incubated at 37°C for 1 h, after which they were added dropwise onto confluent Vero E6 cell or Vero E6-TMPRSS2-T2A-ACE2 cells monolayers in the six-well plates. After incubation at 37°C, 5% (v/v) CO_2 for 1 h, 2 mL of 0.1% (w/v) immunodiffusion agarose (MP Biomedicals) for Munich strain and 0.25% (w/v) immunodiffusion agarose for Delta strain in Dulbecco's modified Eagle's medium (DMEM) (Thermo) with 10% (v/v) FBS and 1x pen-strep was added to each well. The cells were incubated at 37°C, 5% CO_2 for 72 hrs. The agarose overlay was removed and the cell monolayer was fixed with 1 mL/well formaldehyde (Fisher) for 20 min at room temperature. The fixative was discarded and 1 mL/well of 1% (w/v) crystal violet in 10% (v/v) methanol was added. Plates were incubated at room temperature for 20 min and rinsed thoroughly with water. Plaques were then enumerated and the 50% plaque reduction neutralization titer ($PRNT_{50}$) was calculated. A validated SARS-CoV-2 antibody-negative human serum control and a validated NIBSC SARS-CoV-2 plasma control were obtained from the National Institute for Biological Standards and Control, UK) and an uninfected cells control were also used to ensure that virus neutralization by antibodies was specific.

Biological safety

All work with SARS-CoV-2 was conducted under biosafety level-3 (BSL-3) conditions in the University of Pittsburgh Center for Vaccine Research (CVR) and the Regional Biocontainment Laboratory (RBL). Respiratory protection for all personnel when handling infectious samples or working with animals was provided by powered air-purifying respirators (PAPRs; Versaflo TR-300; 3M, St. Paul, MN). Liquid and surface disinfection was performed using Peroxigard disinfectant (1:16 dilution), while solid wastes, caging, and animal wastes were steam-sterilized in an autoclave.

Aerosolization of PiN using a soft-mist inhaler

Nb was eluted and collected in the SEC running buffer (20 mM HEPES, 150 mM NaCl, pH 7.5) and then concentrated to 0.5 mL (1 mg/mL). Nb was aerosolized by using a porTable Soft mist inhaler Pulmospray® (Resyca). Around 0.1–0.15 mL dead volume was observed in the syringe and connector. The aerosols were collected in a 50 mL falcon tube and SEC analysis was performed as described above.

Cryo-electron microscopy data collection and image processing

SARS-CoV-2 HexaPro spike at 1.1 mg/mL was incubated with 1.5-fold molar excess of specified Nbs at room temperature for two hours. 3.5 µL of 1 to 3 dilution sample using HBS buffer with 1% glycerol was applied onto a freshly glow discharged UltraAuFoil R1.2/1.3 grid (300 mesh) and plunge frozen using a vitrobot Mark IV (Thermo Fisher) with a blot force of 0 and 2.5 s blot time at 100% humidity at 4°C. The cryoEM datasets were collected at either CWRU or PNCC.

For CWRU datasets, movie stacks were recorded using an FEI Titan Krios transmission electron microscope G3i operated at 300 keV and equipped with a Gatan K3 direct electron detector and Gatan BioQuantum image filter operated in zero-loss mode with a slit width of 20 eV. Automated data collection was carried out using serialEM at a nominal magnification of 81,000x with a physical pixel size of 1.07 Å/pixel (0.535 Å/pixel at super-resolution) for spike:nanobody complexes and 165,000x with a physical pixel size of 0.52 Å/pixel (0.26 Å/pixel at super-resolution) for RBD:nanobodies complexes. Each movie stack was collected with a dose rate of 18 electron/pixel/s in super-resolution mode and fractionated in 40 frames with two-second exposure, resulting in a total dose of $\sim$31.4 e/Å^2 for 81,000x and in 32 frames with 1.5-second exposure, resulting in a total dose of $\sim$103.4 e/Å^2 for 165,000x. The number of movies for a specified dataset was listed in Table S2. The defocus range was set to between −0.5 and −2 µm.

For PNCC datasets, movie stacks were recorded using an FEI Titan Krios transmission electron microscope G3i operated at 300 keV and equipped with a Gatan K3 direct electron detector and Gatan BioContinuum image filter operated in zero-loss mode with a slit width of 20 eV. Automated data collection was carried out using serialEM at a nominal magnification of 64,000x with a physical pixel size of 1.329 Å/pixel (0.6645 Å/pixel at super-resolution). The dose rate was determined over a sample hole to calculate the exposure time resulting in a total dose of 40 e/Å^2 and the exposures were fractionated into a total of 40 frames. The number of movies for a specified dataset was listed in Table S2. The defocus range was set to between −0.5 and −2 µm.

Image processing was performed on-the-fly using CryoSPARC Live version 3.2. The particles were automatically picked using the blob picker with 240 Å or 100 Å diameter for spike:nanobody or RBD:nanobodies, respectively. Reference-free 2D classification was performed in streaming with 200 classes and limited maximum resolution to 18 Å. Upon the completion of data collection, the selected particles from the good 2D class averages were subjected for another round of 2D classification with 200 classes, and particles from classes with resolution better than 10 Å and ECA less than 2 were selected for subsequent analysis. These 2D classes were submitted for a "rebalance 2D" job type to trim particles from dominant views. The rebalanced particle set was then used for ab-initio reconstruction to generate the initial volume. 3D refinement was first carried out using non-uniform refinement using ab-initio volume as the reference without mask. To resolve the density for nanobodies, an RBD structure (PDB 6M0J) (Lan et al., 2020) was docked into the cryoEM density and the structural model for nanobody was manually placed into the additional density

accounted for nanobodies to ensure the correct orientation. The resulting RBD:nanobody model was used to generate the mask for focused 3D classification in CryoSPARC version 3.3.1 with six classes and target resolution of 6 Å, and PCA was chosen as the initialization mode with the parameter "number of components" set for 2. 3D classes with both RBD and nanobody densities well resolved were selected for sequent new local refinement with the mask around RBD and nanobody. The gold-standard Fourier shell correlation (FSC) of 0.143 criterion was used to report the resolution and the FSC curves were corrected for the effects of a soft mask using high-resolution noise substitution (Scheres and Chen, 2012).

Model building and refinement
PDB entry, 7CAK (Lv et al., 2020), was used as the initial model for spike excluding RBD and the missing fragment for residues 621 to 640 was modeled de novo in Coot. RBD from PDB entry, 6M0J (Lan et al., 2020), was used as the initial model and nanobodies structures were generated using ColabFold (Mirdita et al., 2021). After assembling individual components into a single PDB file, the models were refined into the composite map using phenix.real_space_refine (Afonine et al., 2018). The glycans were built using the carbohydrate module in Coot (Emsley et al., 2010). Models were manually corrected in Coot (version 9.6.0) between rounds of read-space refinement in Phenix. All statistics for structural models were reported in Table S2. Figure panels depicting cryoEM maps or atomic models generated using ChimeraX (Pettersen et al., 2021). Maps colored by local resolution were generated using RELION 3.1 (Zivanov et al., 2018).

Calculation for binding energy contribution
Molecular dynamic (MD) simulations were used to generate short 1 ns trajectory for relative binding energy calculation. Input files for MD simulations of SARS-CoV-2 RBD and nanobody complexes (Table S5) were prepared using tleap. MD simulations were performed using the NAMD and the amber ff19sb (Tian et al., 2020), GLYCAM_06j (Kirschner et al., 2008), ions with the TIP3P water model (Jorgensen et al., 1983). Proteins were solvated in a cubic water box with a 16 Å padding in all directions. Sodium ions and chloride ions were added to achieve a physiological salt condition of 150 mM. The systems were energy minimized for 10,000 steps to remove bad contacts. Then, the systems were equilibrated with all heavy atoms restrained harmonically and the temperature raised 10 K per 10,000 steps starting from 0 to 300 K using temperature reassignment. After reaching the desired temperature, harmonic restraints were gradually reduced using a scale from 1.0 to 0 with a 0.2 decrements for every 50,000 steps. MD simulations were performed under the NPT ensemble (Feller et al., 1995; Martyna et al., 1994). Langevin dynamics was used for constant temperature control, with the value of Langevin coupling coefficient and the Langevin temperature set to 5 ps and 300 K, respectively. The pressure was maintained at 1 atm using the Langevin piston method with a period of 100 fs and decay times of 50 fs. A time step of 2 fs was used for all the simulations by using the SHAKE algorithm (Jean-Paul Ryckaert, 1977) to constrain bonds involving hydrogen atoms.

For each snapshot, every 10 ps of a 1 ns trajectory of SARS-CoV-2 RBD and nanobody complexes, the binding energy of MM/PBSA was calculated using Equations (1) and (2) (Gohlke and Case, 2004; Kollman et al., 2000)

$$\Delta G_{binding} = G_{complex} - G_{RBD} - G_{Nb} \qquad \text{(Equation 1)}$$

$$= \Delta E_{MM} + \Delta G_{GB} + \Delta G_{nonpolar} - T\Delta S \qquad \text{(Equation 2)}$$

where is the molecular mechanic (MM) interaction energy calculated in gas-phase between RBD and nanobody, including electrostatic and van der Waals energies; the desolvation free energy consists of polar (and nonpolar) terms; is the change of conformational entropy on nanobody binding, which was not considered here as the binding epitope on the RBD is very stable and the comparison was performed internally. The decomposition of the binding free energy to the relative energy contribution from individual residues was performed using the MMPBSA.py module in AMBER18 (Miller et al., 2012). The relative contribution to the binding energy from mutated residues observed in VOC were plotted as heatmap.

Crystallographic analysis of psNbs with RBD
The receptor-binding domain (RBD) of the SARS-CoV-2 spike (S) protein (GenBank: QHD43416.1), used in the crystallographic study, was cloned into a customized pFastBac vector (Ekiert et al., 2011), and fused with an N-terminal gp67 signal peptide and C-terminal His$_6$ tag (Yuan et al., 2020). Recombinant bacmids encoding each RBDs were generated using the Bac-to-Bac system (Thermo Fisher) followed by transfection into Sf9 cells using FuGENE HD (Promega) to produce baculoviruses for RBD expression. RBD protein was expressed in High Five cells (Thermo Fisher Scientific) with suspension culture shaking at 110 r.p.m. at 28°C for 72 hours after the baculovirus transduction at an MOI of 5 to 10. Supernatant containing RBD protein was then concentrated using a 10 kDa MW cutoff Centramate cassette (Pall Corporation) followed by affinity chromatography using Ni-NTA resin (QIAGEN) and size exclusion chromatography using a HiLoad Superdex 200 pg column (Cytiva). The purified protein sample was buffer exchanged into 20 mM Tris-HCl pH 7.4 and 150 mM NaCl and concentrated for binding analysis and crystallographic studies.

1-21+SARS-CoV-2 RBD and 2–31+SARS-CoV-2 RBD + CC12.1 complex were formed by mixing each of the protein components in an equimolar ratio and incubating overnight at 4°C. 384 conditions of the JCSG Core Suite (Qiagen) were used for setting-up trays

for screening the 1–21 complex (12 mg/mL) and 2–31 complex (14.3 mg/mL) on our robotic CrystalMation system (Rigaku) at Scripps Research. Crystallization trials were set-up by the vapor diffusion method in sitting drops containing 0.1 μL of protein complex and 0.1 μL of reservoir solution. Crystals appeared on day 3, were harvested on day 12, pre-equilibrated in cryoprotectant containing 0–10% ethylene glycol, and then flash cooled and stored in liquid nitrogen until data collection. X-ray diffraction data were collected at cryogenic temperature (100 K) at beamlines 23-ID-D of the Advanced Photon Source (APS) at Argonne National Laboratory and were collected from crystals grown in drops containing 20% polyethylene glycol 8000, 0.1 M NaCl, 0.1 M CAPS pH 10.5 for the 1–21 complex and drops containing 40% MPD, 0.1M cacodylate pH 6.5, 5% (w/v) polyethylene glycol 8000 for the 2–31 complex. Collected data were processed with HKL2000. X-ray structures were solved by molecular replacement (MR) using PHASER with original MR models for the RBD and Nanobody from PDB 7JMW (Liu et al., 2020b) and PDB 7KN5 (Koenig et al., 2021). Iterative model building and refinement were carried out in COOT and PHENIX, respectively.

RBD epitope analysis by ScanNet
The epitope propensity profile of SARS-CoV-2 RBD (PDB 7jvb) was computed by ScanNet, a state-of-the-art geometric deep learning model for structure-based protein binding site prediction. We used the B-cell epitope network (ScanNet-BCE) without evolutionary information that was not trained on any SARS-CoV-1/2 antibody/antigen complex.

Conservation and ScanNet analysis of viral antigens
Dataset preparation
We collected all viral antibody - antigen complexes in PDB, as listed by SabDab (Dunbar et al., 2014) (release: 10/19/2021). Antigens were clustered at 70% sequence identity with a minimum length coverage of 15% using CD-HIT, the Bio.align pairwise sequence alignment module and CATH domain identifiers. Briefly, we found that (i) ngram-based clustering using CD-HIT with default parameters overestimated the number of clusters, while (ii) computing all the entries of the pairwise sequence similarity matrix was intractable for our set of several thousand structures. We instead proceeded as follows: for a given sequence identity cut-off T (e.g., 100), sequences were clustered with CD-HIT, and the resulting representatives were further clustered at T-20. For each pair of T-representatives with identical CATH identifier or same T-20 cluster, the sequence identity and coverage were evaluated by pairwise alignment and the corresponding T-clusters were merged if necessary. The process was iterated at T = 100%, 95%, 90%, 70% sequence identity cut-offs and yielded satisfactory clusters. We further grouped together the following antigen clusters that had lower sequence identity but high structure similarity: (i) Influenza hemagglutinin from strains H1N1, H3N2, H5N1, H7N9, H2N2 and (ii) Envelope protein of Dengue 1, Dengue 2, Dengue 4 and Zika. Only clusters with at least 7 distinctantibodies were retained for further analysis, yielding 11 viral antigens.

Antibody hit rate calculation
We constructed a multiple sequence alignment for each antigen cluster using MAFFT and selected a representative structure with highest structure coverage and resolution. For each column of the alignment, the antibody hit rate was calculated as the fraction of distinct antibodies binding it. For each complex, we identified the epitope residues as the antigen residues having at least one heavy atom within 4Å of at least one antibody heavy atom. Our analysis was performed on the antigen surface residues (relative accessible surface area ≥ 0.25, computed within the biological assembly for multimeric antigens using Bio.DSSP). Finally, the column-wise antibody hit rate was projected back onto the surface residues representative structure.

Calculation of antigen conservation and epitope propensity
For each representative antigen chain, a multiple sequence alignment was constructed by homology search on the UniRef30_2020_06 sequence database using HHBlits (4 iterations, default parameters). The alignment was deduplicated, hits with high gap content (≥ 25% of the alignment) were discarded and the 10K best hits were retained based on sequence identity. Each sequence was assigned a weight inversely proportional to the number of similar sequences found in the alignment (90% sequence identity cut-off). The amino acid frequency at each site $f_i(a)$ was subsequently calculated and the residue-wise conservation score was defined as $C_i = ln(20) - S(f_i)$ where $S(f_i) = \Sigma_a f_i(a) ln(f_i(a))$ Conservation scores range from 0 to $ln(20) = 2.99$, higher is more conserved. We checked that this protocol correlated well with the ConSurf method based on phylogenetic trees (Ashkenazy et al., 2016). Epitope propensity scores were calculated with ScanNet-BCE.

RMSF calculation
Root mean square fluctuation of each RBD residue was calculated based on 100 ns Molecular Dynamics simulation trajectory. The simulation was run starting from the RBD structure (PDB 6lzg) using Gromacs 2020 version with the CHARMM36m force field. The RBD structure was solvated in transferable intermolecular potential with 3 points (TIP3P) water molecules and ions were added to equalize the total system charge. The steepest descent algorithm was used for initial energy minimization until the system converged at Fmax < 1,000 kJ/(mol · nm). Then water and ions were allowed to equilibrate around the protein in a two-step equilibration process. The first part of equilibration was at a constant number of particles, volume, and temperature (NVT). The second part of equilibration was at a constant number of particles, pressure, and temperature (NPT). For both MD equilibration parts, positional restraints of k = 1,000 kJ/(mol · nm2) were applied to heavy atoms of the protein, and the system was allowed to equilibrate at a reference temperature of 300 K, or reference pressure of 1 bar for 100 ps at a time step of 2 fs. Altogether 10,000 frames were saved for the RMSF

analysis at intervals of 10 ps. To estimate average epitope RMSF, we defined epitope residues as residues with at least one atom within 4Å from the Nb atom and averaged RMSF over epitope residues.

Phylogenetic analysis

The phylogenetic analysis was performed to 1) 19 Sarbecovirus RBD sequences (Figure 1A) 2) 100 psNb CDR3 sequences (Figure S2A) and 3) 32 SEC group B psNb and 3 previously characterized benchmark Nbs (Nb34, Nb95 and Nb105) CDR3 sequences (Figure 4A). Sequences were aligned by MUSCLE with default parameters. The phylogenetic tree was then constructed by the MEGA using the maximized likelihood estimation method.

Sarbecovirus RBD conservation

To calculate Sarbecovirus RBD conservation with respect to SARS-CoV-2, 18 Sarbecovirus RBD sequences mentioned above were aligned to SARS-CoV-2 RBD sequence. After alignment, each SARS-CoV-2 RBD residue was compared to corresponding residue in other RBD sequences. An identical residue to that in SARS-CoV-2 is considered a match. The conservation for each RBD residue is calculated by the number of matches over 18.

psNb epitope clustermap

An RBD residue and an Nb residue were defined in contact if the distance between any pair of their atoms was lower than a threshold of 4 Å. The Nb contact value of each RBD residue is calculated as the sum of all the Nb contacts. psNb classes were determined by using k-means and visual inspection of each complex structure.

Measurement of buried surface area (BSA)

The solvent-accessible surface area (SASA) of molecules was calculated by FreeSASA. The buried surface area in the case of the Nb-RBD complex was then calculated by equation:

Distance between Nb epitope and receptor binding sites

The Nb epitope residues were extracted based on the method described above. The centroid of the Nb epitope residues is defined by the center of mass of atoms. Similarly, the centroid of receptor binding sites (RBS) was extracted. The distance between Nb epitope and RBS was calculated based on the distance between two centroids.

Viral fitness score of epitope residues

The viral fitness score was obtained from (Starr et al., 2020) by evaluating the mutational effects on RBD expression level. The fitness score of each RBD residue is the averaged value of mutating to any other amino acids. The viral fitness score of epitopes was calculated by averaging fitness score over epitope residues.

Glycosylation modeling

Based on the crystal structure of complex ACE2 and SARS-CoV-2 RBD contain seven (N53, N90, N103, N322, N432, N546, N690) and one (N343) N-glycosylation sites, respectively. A heterogeneous glycosylated system was set up for the complex based on previous study (Mehdipour and Hummer, 2021). The glycosylated ACE2:RBD complex was modeled by the Glycan Modeler module of the CHARMM-GUI webserver.

QUANTIFICATION AND STATISTICAL ANALYSIS

GraphPad Prism (version 9.3.1) was used for all statistical calculations. To compare continuous variables, Student's unpaired two-tailed t test was performed between groups. For statistical difference analysis, p values less than 0.05 were considered statistically significant. ns: no significant difference; *: $p < 0.05$; **: $p < 0.01$; ***: $p < 0.001$; ****: $p < 0.0001$.